

Development of 50 cm Diameter  
Hybrid Photo-Detector for Hyper-Kamiokande

Tianmeng Lou  
Department of Physics, University of Tokyo

January 2017

## Abstract

We have developed 50 cm Hybrid Photo-Detector (HPD) as a candidate of photodetectors for Hyper-Kamiokande (HK) which is proposed as a next generation underground large water Cherenkov detector.

An HPD consists of a photocathode glass and a silicon avalanche diode (AD) instead of metal multiple dynodes which are used in a PMT. It is expected that an HPD has better charge resolution because of the high gain at the first amplification stage, and better timing resolution due to its small fluctuation of the drift path in the AD compared to a PMT. In addition, its simpler and axially symmetric structure makes the cost lower, the magnetic field tolerance better and the afterpulse rate lower.

A large diameter AD is required for a large aperture HPD to realize a sufficient collection efficiency. A 50 cm diameter HPD with a 20 mm diameter AD has been selected as our target design. One of the difficulties to develop this type of HPD is the large junction capacitance because of the large area of AD. It worsens the signal to noise ratio. We developed new ADs and preamplifiers to solve this problem and succeed to separate single photoelectron signal and baseline noise.

Using newly developed ADs and preamplifiers, we evaluated the performance of a 50 cm HPD. An HPD has fast enough rise time of 13.4 ns, the charge resolution of 17.7% and timing resolution of 2.7 ns in TTS (FWHM). They are better than other candidate photodetectors. The dark rate of the HPD is  $\sim 10$  kHz at room temperature and it is expected to reach  $\sim 4$  kHz at water temperature in HK operation. The detection efficiency is better than that of SK PMT and the same level of box and line dynode PMT. The output is linear up to 1 MHz and the rate tolerance is sufficient to detect any supernova burst events, while the preamplifier limits the performance. In order to confirm the waterproof assembly of an 50 cm HPD for future long operation in water, we do the waterproof HPD test and it works stably for two weeks with applying high voltage.

The basic configuration of a 50 cm HPD is confirmed as the inner photodetector of HK and after the R&D of practical application, a 50 cm HPD will be ready for use in a water Cherenkov detector.

# Contents

<b>Abstract</b>	<b>1</b>
<b>Contents</b>	<b>2</b>
<b>List of Figures</b>	<b>5</b>
<b>List of Tables</b>	<b>6</b>
<b>1 Introduction</b>	<b>7</b>
1.1 Physics motivation . . . . .	7
1.1.1 Neutrino Oscillation . . . . .	7
1.1.2 Mass hierarchy . . . . .	8
1.1.3 Leptonic CP violation . . . . .	9
1.1.4 Nucleon decay . . . . .	10
1.1.5 Neutrino astronomy . . . . .	10
1.2 Current neutrino experiments . . . . .	11
1.2.1 Super-Kamiokande . . . . .	11
1.2.2 T2K experiment . . . . .	12
1.3 Hyper-Kamiokande project . . . . .	13
1.3.1 Overview of HK . . . . .	13
1.3.2 Detection principle . . . . .	15
<b>2 Development of new photodetectors for Hyper-K</b>	<b>18</b>
2.1 R&D motivation and requirements for Hyper-K photodetectors . . . . .	18
2.2 Photodetector candidates for Hyper-K . . . . .	20
2.2.1 Box&Line PMT . . . . .	20
2.2.2 Hybrid Photo-Detector . . . . .	21
2.2.3 Goals of this thesis . . . . .	22
<b>3 Development of 50 cm HPD with 20 mm diameter avalanche diode</b>	<b>24</b>
3.1 Difficulty of using 20 mm diameter AD . . . . .	24
3.2 Improvement of AD . . . . .	25
3.2.1 Development of low capacitance AD . . . . .	25
3.2.2 Application of segmented AD . . . . .	25

3.3	Improvement of preamplifier . . . . .	27
3.3.1	Difficulties in preamplifier development . . . . .	27
3.3.2	Sequence of preamplifier development . . . . .	28
3.3.3	Developed preamplifiers . . . . .	30
3.4	Summary of developed HPD types . . . . .	30
<b>4</b>	<b>Performance evaluation of 50 cm HPD</b>	<b>33</b>
4.1	Setup for performance evaluation . . . . .	33
4.2	Waveform . . . . .	35
4.3	Gain . . . . .	36
4.4	Charge resolution . . . . .	38
4.5	Timing resolution . . . . .	39
4.6	Dark rate . . . . .	43
4.7	Photon detection efficiency . . . . .	44
4.8	Afterpulse . . . . .	45
4.9	Rate tolerance . . . . .	46
4.10	Viability test of an 50 cm HPD in water . . . . .	47
<b>5</b>	<b>Conclusion</b>	<b>50</b>
5.1	Summary of performance evaluation . . . . .	50
5.2	Remaining issues . . . . .	51
5.3	Future prospect . . . . .	52
	<b>Acknowledgements</b>	<b>54</b>
<b>A</b>	<b>Long term measurement of dark rate of Hyper-K photodetectors</b>	<b>55</b>
A.1	Setup . . . . .	55
A.2	Result from October 2015 to September 2016 . . . . .	57
A.3	Result from August 2016 to November 2016 . . . . .	58

# List of Figures

1.1	Schematic view of neutrino mass hierarchy. . . . .	9
1.2	A schematic view of Super-Kamiokande. . . . .	12
1.3	Inside of Super-Kamiokande. . . . .	12
1.4	Configuration of the detectors of T2K experiment. . . . .	13
1.5	View of the T2K experiment . . . . .	13
1.6	Off-axis fluxes and oscillation probabilities. . . . .	13
1.7	The schematic view of near detectors. . . . .	13
1.8	The schematic view of Hyper-Kamiokande detector. . . . .	14
1.9	The example of neutrino interactions. The left (right) diagram shows the charged (neutral) current interaction of neutrino-nucleon scattering. . . . .	16
1.10	Image of the emitted Cherenkov light. . . . .	17
1.11	Image of the Cherenkov ring. . . . .	17
1.12	The difference of the Cherenkov rings in SK. Right shows the ring of a muon and left shows that of an electron. The ring of an electron is more indistinct than that of muon due to the multiple scattering in water. . . . .	17
2.1	Venetian blind PMT / Super-Kamiokande PMT (SK PMT) / Hamamatsu R3600 NQE. . . . .	20
2.2	Box&Line PMT (B&L PMT) / Hamamatsu R12860 HQE. . . . .	21
2.3	The principle of an HPD amplification and typical values of the 50cm HPD. . . . .	22
2.4	Summary of HPD development. . . . .	23
3.1	The principle of current noise increase due to the large junction capacitance of an AD and a trans-impedance amplifier. . . . .	25
3.2	Schematic view of segmented AD and readout system. . . . .	27
3.3	The AD junction capacitance dependency of the noise level in pulse height (left) and in charge (right). . . . .	27
3.4	Description of problems to develop the preamplifier of 50 cm HPD with 20 mm diameter AD. . . . .	28
3.5	Left (right) is the image (circuit diagram) of the preamplifier test board. . . . .	29
3.6	The output signal waveform of a preamplifier at the pre-test. . . . .	29

3.7	Comparison of waveform and charge distribution between type I and II preamplifier. . . . .	31
3.8	The comparison of old and new preamp in waveform. . . . .	31
3.9	The comparison of old and new preamp in charge distribution. . . . .	31
3.10	Circuit diagram of type I preamplifier. . . . .	32
3.11	Circuit diagram of type II preamplifier. . . . .	32
4.1	The overview of the whole system to operate an HPD and data acquisition. . . . .	34
4.2	A picture of the socket assembly of HPD. . . . .	34
4.3	Pictures of the HV-LV control power supply. . . . .	35
4.4	Waveform of each photodetector. . . . .	36
4.5	Measured total gain of 1ch HPD with preamplifier as a function of the HV with fixed AD bias voltage of 520 kV. . . . .	37
4.6	Measured total gain of 1ch HPD with preamplifier as a function of the AD bias voltage with fixed HV of 8 kV. . . . .	37
4.7	1 p.e. charge distribution of 5ch, 2ch, 1ch HPD by single channel readout (left) and sum-amp readout (right). . . . .	38
4.8	Definition of $\mu_{1\text{ p.e.}}$ , $\mu_{\text{ped}}$ , $\sigma_{1\text{ p.e.}}$ , $\sigma_{\text{ped}}$ , peak, valley in charge distribution. . . . .	39
4.9	Definition of transit time. . . . .	40
4.10	Single photo-electron transit time spread (TTS) of each photodetectors. Left (right) figure contains TTS of HPD with the bias voltage $\sim 520\text{ V}$ ( $\sim 570\text{V}$ ). . . . .	40
4.11	Setup of the timing resolution measurement. . . . .	41
4.12	The TQ-map (time charge map) of 1ch HPD. . . . .	42
4.13	Multi photo-electron transit time spread (TTS) of each photodetectors. . . . .	42
4.14	The dark rate of 1ch and 2ch HPD as a function of the threshold. The dotted red line shows the dark rate of each channel of 2ch HPD and the solid red line shows the sum of tow dotted red line. . . . .	43
4.15	The measured relative total detection efficiency (= relative collection efficiency (CE) $\times$ quantum efficiency (QE)), QE measured by Hamamatsu photonics and calculated relative CE. . . . .	44
4.16	The charge distrubition and trigger efficiency of an HPD and a B&L PMT. . . . .	45
4.17	The afterpulse rate of each photodetector between -5 to 50 $\mu\text{s}$ time windows from main pulse. . . . .	46
4.18	The output signal stability of HPD in charge and pulse height. . . . .	47
4.19	The schematic view of EGADS tank (a 200-ton water tank). . . . .	48
4.20	The extend elevation of EGADS tank. Green circles show the places planning to install 50 cm HPDs. . . . .	48
4.21	The waterproof HPDs and the picture of operation in water. . . . .	48
4.22	1 p.e. and multi p.e. signal of a waterproof 50 cm HPD. . . . .	48
4.23	The multi p.e. charge distribution of a waterproof 50 cm HPD and charge of each number of photo-electron peaks. . . . .	49

4.24	The variation of dark rate and water temperature during continuous operation of a waterproof HPD. . . . .	49
4.25	The relationship of a temperature and a dark rate of a waterproof HPD. . . . .	49
5.1	The shape of the glass bulb. . . . .	52
A.1	Image of setup in dark room. . . . .	56
A.2	The setup of DAQ system for long measurement. . . . .	56
A.3	The time variation of gain (upper) and dark rate (lower). The left column shows the whole history of gain and dark rate and the right column shows the history after May 2016. . . . .	57
A.4	The time variation of the dark rate after installing newly developed B&L PMTs . . . . .	58
A.5	The temperature dependency of PMT dark rate. . . . .	59
A.6	The high voltage and trigger threshold level dependency of the dark rate. . . . .	60

# List of Tables

1.1	The parameters of Hyper-Kamiokande. . . . .	14
2.1	Minimum requirements for the Hyper-K inner photodetectors, based on the performance of SK PMT(R3600) and HK. . . . .	19
2.2	The performance summary of SK PMT and B&L PMT. . . . .	21
3.1	Summary of AD types and typical values. 1ch AD means not- segmented AD. . . . .	26
3.2	Summary of HPD types and evaluation using each type of HPD. . . . .	30
3.3	Summary of developed preamplifiers. . . . .	31
4.1	Summary of rise time, fall time and FWHM of each photodetector. . . . .	35
4.2	Summary of 1 p.e. resolution, noise level, peak to valley ratio of each photodetector. . . . .	39
4.3	The summary of single photoelectron timing resolution for each photodetectors. . . . .	41
4.4	The rate of afterpulse to mainpulse for each photodetector. . . . .	46
5.1	The summary of the evaluated performances of the 50 cm HPDs and comparison with SK PMT and B&L PMT. . . . .	51
A.1	Summary of the type of measured photodetectors and averaged dark rate after stabilization. WPASSY is short for waterproof assembly. . . . .	58

# Chapter 1

## Introduction

In this chapter, we describe the physics targets which can be approached by a large water Cherenkov detector in Section 1.1. Then, we introduce the current experiments in Section 1.2 and the future project in Section 1.3.

### 1.1 Physics motivation

#### 1.1.1 Neutrino Oscillation

A neutrino is one of the elementary particles interacting only via weak force and gravity. In the standard model, there are three types of neutrinos, electron neutrino( $\nu_e$ ), muon neutrino( $\nu_\mu$ ), tau neutrino( $\nu_\tau$ ), and their masses are assumed to be zero. However, In 1998, neutrino oscillation was discovered via the measurement of the atmospheric neutrinos in Super-Kamiokande (SK). This implies that neutrinos have non zero masses. By exploring the properties of neutrino in detail, it may be possible to construct the physics theory beyond the standard model.

Neutrino oscillation is a phenomenon that a neutrino with a specific lepton flavor ( $e$ ,  $\mu$ , or  $\tau$ ) can be observed as a neutrino with a different flavor after a spatial propagation. Assuming that neutrinos have non zero masses, three-generation neutrino mixing can be described as

$$|\nu_\alpha\rangle = \sum_i U_{\alpha i} |\nu_i\rangle \quad (1.1)$$

where  $|\nu_\alpha\rangle$  ( $\alpha = e, \mu, \tau$ ) are eigenstates of weak interaction,  $|\nu_i\rangle$  ( $i = 1, 2, 3$ ) are mass eigenstates, and  $U_{\alpha i}$  is an element of  $3 \times 3$  unitary matrix called Maki-

Nakagawa-Sakata (MNS) matrix [1], given as

$$\begin{aligned}
U &= \begin{bmatrix} 1 & 0 & 0 \\ 0 & c_{23} & s_{23} \\ 0 & -s_{23} & c_{23} \end{bmatrix} \begin{bmatrix} c_{13} & 0 & s_{13}e^{-i\delta_{CP}} \\ 0 & 1 & 0 \\ -s_{13}e^{i\delta_{CP}} & 0 & c_{13} \end{bmatrix} \begin{bmatrix} c_{12} & s_{12} & 0 \\ -s_{12} & c_{12} & 0 \\ 0 & 0 & 1 \end{bmatrix} \\
&= \begin{bmatrix} c_{12}c_{13} & c_{13}s_{12} & s_{13}e^{-i\delta_{CP}} \\ -c_{12}s_{13}s_{23}e^{i\delta_{CP}} - c_{23}s_{12} & c_{12}c_{23} - s_{12}s_{13}s_{23}e^{i\delta_{CP}} & c_{13}s_{23} \\ -c_{12}c_{23}s_{13}e^{i\delta_{CP}} + s_{12}s_{23} & -c_{12}s_{23} - c_{23}s_{12}s_{13}e^{i\delta_{CP}} & c_{13}c_{23} \end{bmatrix} \quad (1.2)
\end{aligned}$$

where  $c_{ij} = \cos \theta_{ij}$ ,  $s_{ij} = \sin \theta_{ij}$ ,  $\theta$  is a mixing angle, and  $\delta_{CP}$  is a CP violating phase.

In vacuum, the oscillation probability between two flavors after traveling the distance L is described as

$$\begin{aligned}
P(\nu_\alpha \rightarrow \nu_\beta) &= \left| \sum_i U_{\alpha i}^* U_{\beta i} e^{-i \frac{m_i^2}{2E_\nu} L} \right|^2 \\
&= \delta_{\alpha\beta} - 4 \sum_{i>j} \text{Re}(U_{\alpha i}^* U_{\alpha j} U_{\beta i} U_{\beta j}^*) \sin^2 \left( \frac{\Delta m_{ij}^2 L}{4E_\nu} \right) \\
&\quad + 2 \sum_{i>j} \text{Im}(U_{\alpha i}^* U_{\alpha j} U_{\beta i} U_{\beta j}^*) \sin \left( \frac{\Delta m_{ij}^2 L}{2E_\nu} \right) \quad (1.3)
\end{aligned}$$

where E is energy of the neutrino and  $\Delta m_{ij}^2 = m_i^2 - m_j^2$ .

As described above, neutrino oscillation between three-generation depend on six parameters: two mass-squared differences ( $\Delta m_{21}^2$ ,  $\Delta m_{32}^2$ ), three mixing angles ( $\theta_{12}$ ,  $\theta_{23}$ ,  $\theta_{13}$ ) and one CP phase ( $\delta_{CP}$ ). At present,  $\theta_{12}$  and  $\Delta m_{21}^2$  have been measured by solar [2] and reactor [3, 4] neutrino experiments.  $\theta_{23}$  and  $|\Delta m_{32}^2|$  (absolute value) have been measured by atmospheric [5, 6], accelerator [7, 8, 9] and reactor [10] neutrino experiments.  $\theta_{13}$  has also been measured by accelerator [11] and reactor experiments [10]. The sign of  $\Delta m_{32}^2$  and the value of  $\delta_{CP}$  are left to be determined.

### 1.1.2 Mass hierarchy

Neutrino oscillation experiments measure the mass square differences ( $\Delta m_{21}^2$  and  $\Delta m_{32}^2$ ) instead of the absolute masses. In vacuum, only the absolute value of the mass square differences can be measured. The sign can be measured in matter because the electrons in matter change the neutrino oscillation probabilities by Mikheyev-Smirnov-Wolfenstein mechanism [12, 13].

Currently, the sign of  $\Delta m_{21}^2$  is determined by the measurement of solar neutrino, however that of  $\Delta m_{32}^2$  is still unknown. Therefore, the ordering of  $m_1$ ,  $m_2$  and  $m_3$  is not determined. This is called the neutrino mass hierarchy problem. We can consider two patterns of the mass ordering: normal hierarchy (NH), e.g.,  $m_3 \gg m_2 > m_1$  and inverted hierarchy (IH), e.g.,  $m_2 > m_1 \gg m_3$  as shown in Fig. 1.1.

It is expected that the neutrino mass hierarchy will be determined by future neutrino experiments, e.g., accelerator-based long-baseline experiments like NOvA, DUNE and T2HK, atmospheric neutrino experiments like Hyper-K and PINGU and reactor neutrino experiments like JUNO.

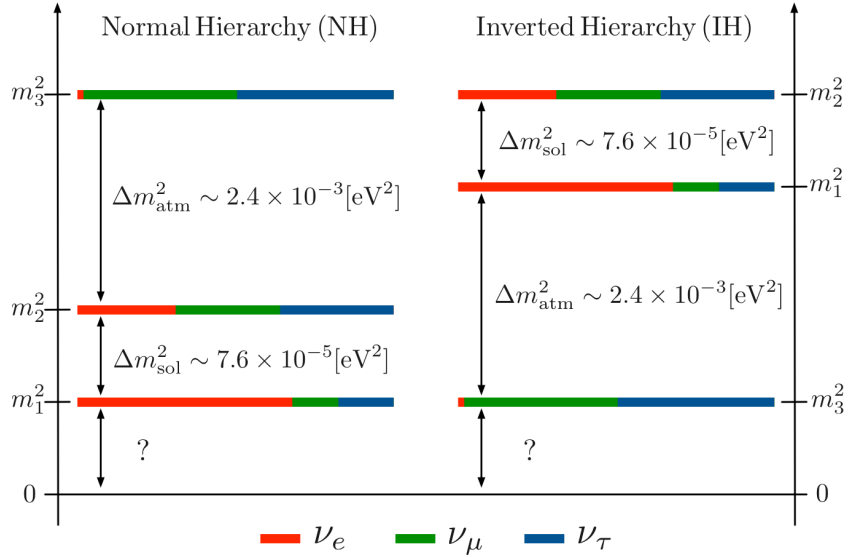


Figure 1.1: Schematic view of neutrino mass hierarchy.

### 1.1.3 Leptonic CP violation

Why our universe mainly consists of not antimatter (antibaryons) but matter (baryons) is one of the unsolved problems in physics. To create the baryonic asymmetry, the Sakharov conditions [14] must be satisfied, which contains the existence of CP violation. The CP violation in quark sector has been observed in the experiments of K [15] or B [16] mesons. However, it is not sufficient to explain the matter-antimatter asymmetry. The CP violation in lepton sector is proposed as the other source of the baryonic asymmetry and neutrino experiments aim to observe the CP violating phase.

The oscillation probability from  $\nu_\mu$  to  $\nu_e$  is expressed, to the first order of

the matter effect,

$$\begin{aligned}
P(\nu_\mu \rightarrow \nu_e) = & 4c_{13}^2 s_{13}^2 s_{23}^2 \cdot \sin^2 \Delta_{31} \\
& + 8c_{13}^2 s_{12} s_{13} s_{23} (c_{12} c_{23} \cos \delta_{\text{CP}} - s_{12} s_{13} s_{23}) \cdot \cos \Delta_{32} \cdot \sin \Delta_{31} \cdot \sin \Delta_{21} \\
& - 8c_{13}^2 c_{12} c_{23} s_{12} s_{13} s_{23} \sin \delta_{\text{CP}} \cdot \sin \Delta_{32} \cdot \sin \Delta_{31} \cdot \sin \Delta_{21} \\
& + 4s_{12}^2 c_{13}^2 (c_{12}^2 c_{23}^2 + s_{12}^2 s_{23}^2 s_{13}^2 - 2c_{12} c_{23} s_{12} s_{23} s_{13} \cos \delta_{\text{CP}}) \cdot \sin^2 \Delta_{21} \\
& - 8c_{13}^2 s_{13}^2 s_{23}^2 \cdot \frac{aL}{4E_\nu} (1 - 2s_{13}^2) \cdot \cos \Delta_{32} \cdot \sin \Delta_{31} \\
& + 8c_{13}^2 s_{13}^2 s_{23}^2 \frac{a}{\Delta m_{31}^2} (1 - 2s_{13}^2) \cdot \sin^2 \Delta_{31}, \tag{1.4}
\end{aligned}$$

where  $\Delta_{ij}$  is  $\Delta m_{ij}^2 L/4E_\nu$ , and  $a[\text{eV}^2] = 7.56 \times 10^{-5} \times \rho[\text{g}/\text{cm}^3] \times E_\nu[\text{GeV}]$ . The probability from  $\bar{\nu}_\mu$  to  $\bar{\nu}_e$  is obtained by replacing  $\delta_{\text{CP}} \rightarrow -\delta_{\text{CP}}$  and  $a \rightarrow -a$ . If  $\delta_{\text{CP}}$  is non-zero, the third term of Eq. 1.4 flips its sign between  $\nu$  and  $\bar{\nu}$  due to CP asymmetry (the last two terms also flip its sign due to the matter effect). Therefore, the effect of the CP phase can be observed by measuring  $\Delta P_{\mu e} \equiv P(\nu_\mu \rightarrow \nu_e) - P(\bar{\nu}_\mu \rightarrow \bar{\nu}_e)$ .

To determine the CP phase, we need more statistics of neutrino events than that expected with T2K. A water Cherenkov detector with larger volume than SK and higher intensity neutrino beam are required.

### 1.1.4 Nucleon decay

Grand Unified Theories (GUTs) are proposed models in which the three fundamental interactions of the Standard Model, i.e, the electromagnetic, weak, and strong interactions, are integrated into one single force and quarks and leptons are unified. Most GUTs predict baryon number violation, and nucleon decays as a consequence.

Nucleon decays have never been observed experimentally and only lifetime limits are set mainly by SK, the largest detector for the observation of nucleon decay in the world. SK has been searching for nucleon decay events since 1996. The current lower limits of proton lifetime are  $1.6 \times 10^{34}$  years for  $p \rightarrow e^+ + \pi^0$ ,  $7.7 \times 10^{33}$  years for  $p \rightarrow \mu^+ + \pi^0$  [17] and  $5.9 \times 10^{33}$  for  $p \rightarrow \bar{\nu} + K^+$  [18].

In order to extend the sensitivity beyond these limits, a much larger number of nucleons than SK and sufficient reconstruction ability to extract signals and suppress backgrounds are necessary.

### 1.1.5 Neutrino astronomy

Neutrino astronomy is one branch of astronomy using neutrinos as the probe to observe astronomical objects. The main sources of neutrinos observed in SK or HK are the sun and supernovae.

The neutrinos from the sun are created with the nuclear fusion reactions, that are called the pp-chain and the CNO cycle. These processes are described with the standard solar model (SSM). Because of its rare reaction rate, neutrinos

can probe the internal state of the sun in real time. Therefore, we can test the SSM predictions by observing the solar neutrinos. Another motivation is the study of neutrino properties themselves. The neutrino oscillation parameter  $\theta_{12}$ ,  $\Delta m_{12}^2$  are determined by observing the solar neutrinos.

The supernova, the last process in the evolution of massive stars ( $> 8M_{\odot}$ ), will emit numerous neutrinos called the supernova burst neutrinos. From SN1987A, the Kamiokande, IMB, and Baksan experiments observed 25 neutrino events and this discovery starts neutrino astronomy. No supernova burst neutrino has been observed since SN1987A, but recently it is said that Betelgeuse might explode and emit neutrinos.

Another observation is the supernova relic neutrinos (SRN), produced by all past supernova explosions since the beginning of the universe and diffused. SRN contains the information of the star formation rate, energy spectrum of supernova burst neutrinos, and black hole or neutron star formations.

To detect the supernova neutrinos, we need a large detector which can observe MeV order neutrino. In addition, the multi-messenger observation with visible light, gamma-ray, x-ray and gravitational wave will also reveal the supernova explosion in details.

## 1.2 Current neutrino experiments

### 1.2.1 Super-Kamiokande

Super-Kamiokande (SK) is a large water Cherenkov detector located at 1,000 meter underground in the Kamioka-mine, Hida-city, Gifu, Japan. Fig. 1.2 shows a schematic view of SK. The detector consists of a cylindrical tank, 39.3m diameter and 41.4m tall, filled with 50,000 tons of ultra pure water. Fig. 1.3 shows the inside view of SK. Eleven thousand and two hundred of 50 cm photomultiplier tubes (PMTs) are used for the inner detector and one thousand one hundred and eighty five of 20cm PMT are used for the outer detector to veto the cosmic muons. It measures the multiple kinds of neutrinos and nucleon decay by detecting Cherenkov light emitted by a charged particle produced in water. SK is characterized by its wide energy range between MeV to TeV and has accomplished many significant achievements, most notably the observation of neutrino oscillation and the measurement of neutrino oscillation parameters.

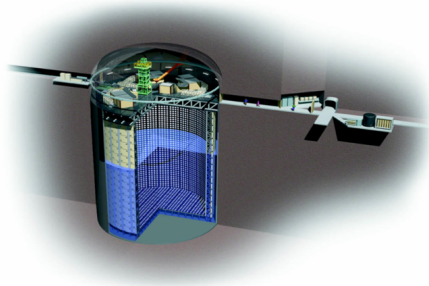


Figure 1.2: A schematic view of Super-Kamiokande.

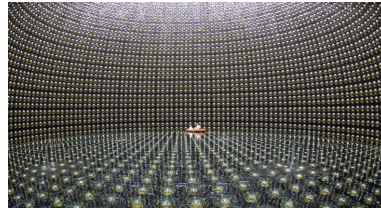


Figure 1.3: Inside of Super-Kamiokande.

### 1.2.2 T2K experiment

T2K (Tokai to Kamioka) experiment is a long baseline neutrino oscillation experiment, started from 2009 in order to measure  $\theta_{13}$ ,  $\theta_{23}$ ,  $\Delta m_{32}^2$  and  $\delta_{CP}$ . The  $\nu_\mu$  ( $\bar{\nu}_\mu$ ) beam produced by J-PARC in Tokai, Ibaraki, Japan is detected by near detectors in J-PARC and SK in Kamioka, which is 295 km away, as a far detector to measure the probability of  $\nu_\mu \rightarrow \nu_e$  ( $\bar{\nu}_\mu \rightarrow \bar{\nu}_e$ ) appearance and  $\nu_\mu \rightarrow \nu_\mu$  ( $\bar{\nu}_\mu \rightarrow \bar{\nu}_\mu$ ) disappearance.

To create the J-PARC neutrino beam, 30 GeV protons from the synchrotron accelerator strike a graphite target and produce pions. They are focused by the electromagnetic horns, decay in a 96 m decay volume and produce a neutrino beam. The beam is directed 2.5° degrees away from the far detector to optimize the neutrino energy spectrum which has a peak at the first oscillation maximum, around 0.6 GeV as shown in Fig. 1.6.

Near detector consists of on axis and off-axis detectors as shown in Fig. 1.7. The on axis near detector, INGRID and Proton Module, measure the neutrino event rate and the direction of the neutrino beam. They also measure the neutrino cross section to study the neutrino interaction. The off-axis near detector, ND280 (Near Detector at 280 m from production target), measures the neutrino event rate and the cross section of the neutrino interaction.

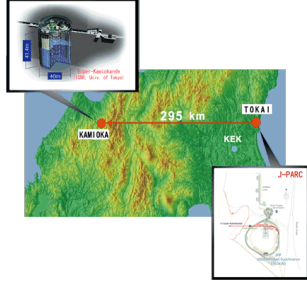


Figure 1.4: Configuration of the detectors of T2K experiment.



Figure 1.5: View of the T2K experiment

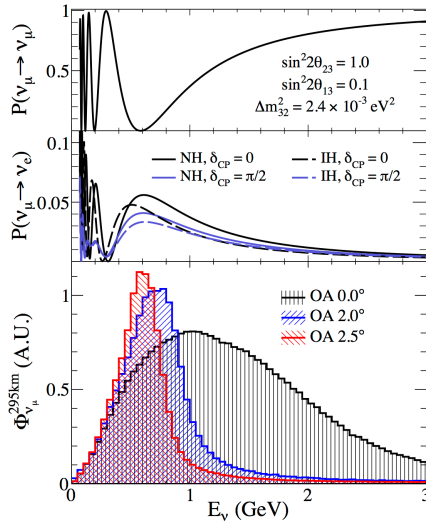


Figure 1.6: Off-axis fluxes and oscillation probabilities.

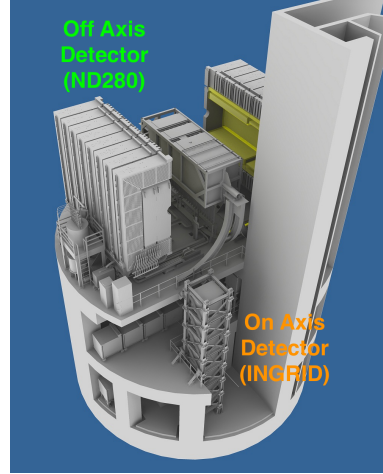


Figure 1.7: The schematic view of near detectors.

## 1.3 Hyper-Kamiokande project

### 1.3.1 Overview of HK

Hyper-Kamiokande (HK) is a next generation underground large water Cherenkov detector, based on the SK [19]. Fig. 1.8 shows the schematic view of HK and the parameters of HK is summarized in Table 1.1. HK consists of two cylindrical water tanks which are 60 m in height and 74 m in diameter. Its fiducial (total) mass is 0.37 (0.52) Mtons, which is 17 times of that of SK. Forty thousand of photodetectors with 50 cm diameter will be used in the inner detectors and six thousand and seven hundred of photodetectors with 20 cm diameter will be used

in outer detectors to veto cosmic-ray muons.

HK aims to measure rich physics targets with much higher statistics and sensitive detectors than SK, i.e., precise study of neutrino oscillation (determination of mass hierarchy and  $\theta_{23}$  octant) and the measurement of CP violation in lepton sector using beam and atmospheric neutrinos, search for proton decay to verify grand unified theory, observation of astrophysical neutrino and neutrino geophysics.

The candidate site is Kamioka mine, Gifu, Japan because of much water, hard bedrocks and the limitation of off axis angle from J-PARC neutrino beam. The measurement with the first tank will start from 2025 and that with the second tank will start from 6 years after the beginning of that with the first tank.

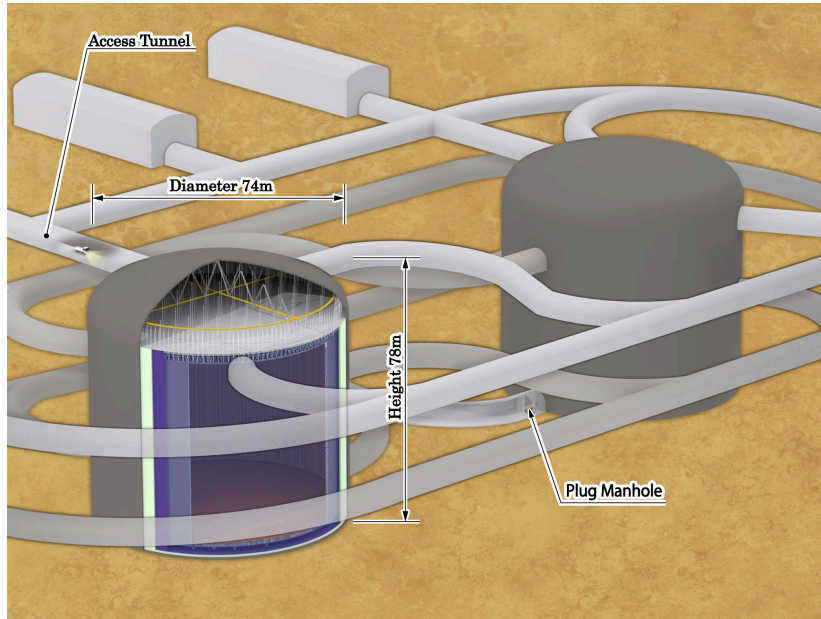


Figure 1.8: The schematice view of Hyper-Kamiokande detector.

Table 1.1: The parameters of Hyper-Kamiokande.

Parameter	Value of 1 tank	Value of 2 tank
Diameter of water tank [m]	74	74
Height of water tank [m]	60	60
Total volume [Mton]	0.258	0.516
Fiducial volume [Mton]	0.187	0.374
Number of inner photodetectors	40,000	80,000
Number of outer photodetectors	6,700	13,400

### 1.3.2 Detection principle

#### Neutrino interaction

There are two kinds of neutrino interaction as shown in Fig. 1.9. One is charged current (CC) interaction which exchange a  $W^\pm$  and a neutrino converts into a corresponding charged lepton like  $\nu_e + N \rightarrow e + N'$ . The other is neutral current (NC) interaction which exchange a  $Z^0$  and a neutrino does not convert like  $\nu + N \rightarrow \nu + N'$ . Only energy and momentum are exchanged.

In the accelerator or atmospheric neutrino experiments, which energy regime is O(1 GeV), neutrino-nucleus interactions become dominant. These interactions can be described by two steps. First, a neutrino interacts with a nucleon in a nucleus by exchanging weak bosons and produces secondary particles. Then, these particles interact with the nucleons in nucleus. Neutrino-nucleus interactions can be divided into four classes on the basis of the interaction product:

- quasi-elastic scattering ( $\nu + N \rightarrow l + N'$ )
- single meson production via baryon resonances ( $\nu + N \rightarrow l + N' + m$ )
- coherent pion production ( $\nu + A \rightarrow l + A + \pi$ )
- deep inelastic scattering ( $\nu + N \rightarrow l + N' + \text{hadrons}$ )

where N and N' are nucleons (proton or neutron), l is a lepton, m is a meson and A is a nucleus. For a neutrino which energy is less than 1 GeV like T2K neutrino beam, CCQE interaction becomes dominant.

In HK, the informations of the initial neutrino can be reconstructed by detecting the Cherenkov light emitted by the charged particles produced in water. For example, assuming a charged current quasi-elastic (CCQE) interaction of the accelerator neutrino, the neutrino energy ( $E_\nu^{\text{rec}}$ ) is reconstructed from the energy of the final state charged lepton ( $E_l$ ) and the angle between the neutrino beam and the charged lepton directions ( $\theta_l$ ) as

$$E_\nu^{\text{rec}} = \frac{2(m_n - V)E_l + m_p^2 - (m_n - V)^2 - m_l^2}{2(m_n - V - E_l + p_l \cos \theta_l)} \quad (1.5)$$

where  $m_n$ ,  $m_p$ ,  $m_l$  are the mass of neutron, proton, and charged lepton,  $p_l$  is the momentum of charged lepton and  $V$  is the nuclear potential energy (27 MeV).

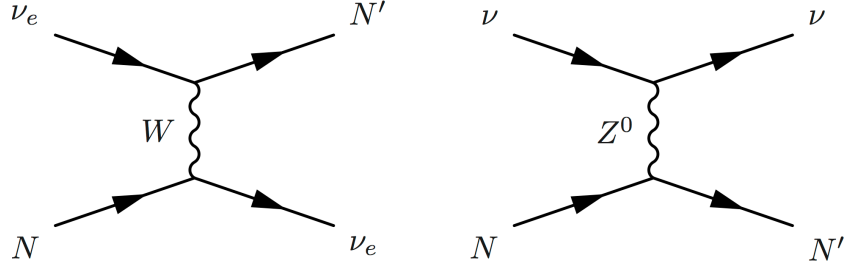


Figure 1.9: The example of neutrino interactions. The left (right) diagram shows the charged (neutral) current interaction of neutrino-nucleon scattering.

### Cherenkov light

When a charged particle passes through a dielectric medium faster than the phase velocity of light in that medium, Cherenkov light is emitted as shown in Fig. 1.10. The angle between the direction of the traveling charged particle and the Cherenkov light, called the Cherenkov angle ( $\theta$ ), is written as

$$\cos \theta = \frac{1}{n\beta} \quad (1.6)$$

where  $\beta$  is the velocity of the charged particle in unit of  $c$  ( $\beta = v/c$ ) and  $n$  is the refractive index. In water,  $n$  is 1.33 and the Cherenkov angle becomes  $\sim 41$  degrees in extreme relativistic limit.

Following Eq. 1.6 and  $0 \leq \cos \theta \leq 1$ , the lower limit of the velocity to emit Cherenkov light becomes  $\beta = 1/n$  and the corresponding energy is

$$E_{\text{thr}} = \frac{mc^2}{\sqrt{1-\beta^2}} = \frac{mc^2}{\sqrt{1-(1/n)^2}} \simeq 1.5 mc^2 \text{ (in water)} \quad (1.7)$$

where  $m$  is the mass of the charged particle. For electron,  $E_{\text{thr}}$  becomes 0.77 MeV. The particle which energy is below  $E_{\text{thr}}$  cannot be observed.

As shown in Fig. 1.11, when the charged particle stops inside the water tank, Cherenkov light projected on the wall forms a donut shape called the Cherenkov ring and its shape depends on the particle type (Fig. 1.12). The Cherenkov light is detected by photodetectors installed on the wall and each photodetector sends its timing and intensity information. The ring image is reconstructed by these informations and the vertex point, event time, direction, type and energy of the charged particle and neutrino can then be determined.

The number of Cherenkov photons  $dN$  generated per unit distance  $dx$  and unit wavelength  $d\lambda$  of the charged particle is written as

$$\frac{d^2N}{dx d\lambda} = \frac{2\pi\alpha z^2}{\lambda^2} \left(1 - \frac{1}{n^2\beta^2}\right) = \frac{2\pi\alpha z^2}{\lambda^2} \sin^2 \theta \quad (1.8)$$

where  $\alpha$  is the fine structure constant ( $\sim 1/137$ ) and  $z$  is the electric charge of incident particle. By integrating the wavelength over 300  $\sim$  600 nm, which is

the sensitive range of a photodetector for HK and considering the velocity of  $\beta \simeq 1$ , the number of emitted Cherenkov photons per unit of distance becomes

$$\frac{dN}{dx} \simeq 340z^2 \text{ [photons/cm]}. \quad (1.9)$$

Considering an electron with the energy of 3 MeV, which is a required lower energy threshold in HK, an electron loses  $\sim 2$  MeV/cm in water from the Bethe-Bloch equation and the range to reach  $E_{\text{thr}}$  becomes  $\sim 1$  cm. Then, the total emitted Cherenkov photons are  $\sim 340$ . Considering the water transparency, the remaining number of photons becomes  $340/2.7 = 126$ . Assuming a 40% photo-coverage and a 30% quantum efficiency of a photodetector, the number of photodetector which can observe Cherenkov photons is  $\sim 15$  ( $\sim 5$  hit photodetectors/MeV). Therefore, the performance of photodetectors becomes critical especially for the study of low energy physics and proton decay.

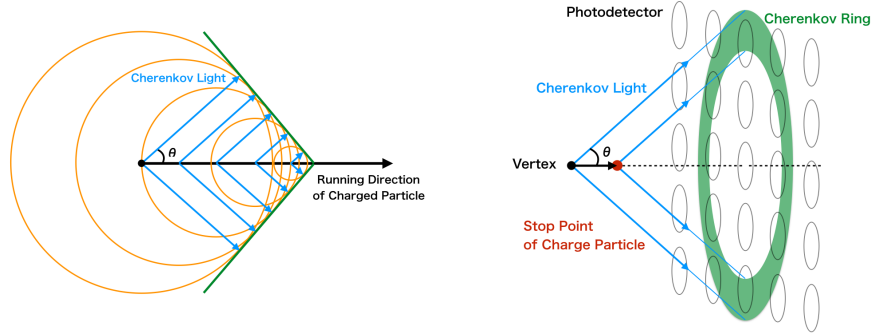


Figure 1.10: Image of the emitted Cherenkov light.

Figure 1.11: Image of the Cherenkov ring.

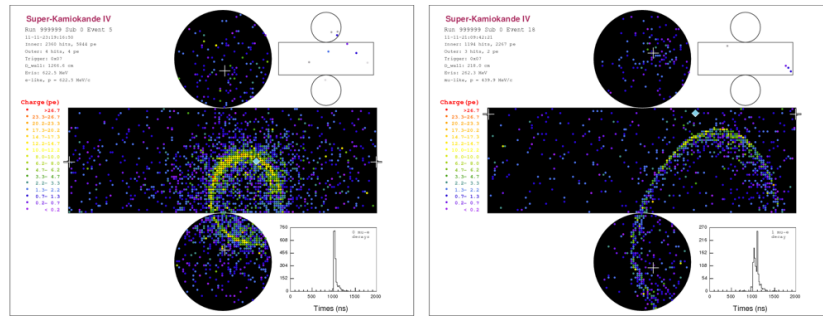


Figure 1.12: The difference of the Cherenkov rings in SK. Right shows the ring of a muon and left shows that of an electron. The ring of an electron is more indistinct than that of muon due to the multiple scattering in water.

## Chapter 2

# Development of new photodetectors for Hyper-K

### 2.1 R&D motivation and requirements for Hyper-K photodetectors

The performances of photo-detectors are one of the most influential factors to determine the performance of a water Cherenkov detector. In Super-K, 50 cm Venetian Blind dynode type PMT (SK PMT) is used as photo-detectors and its performance is well confirmed. However, SK PMT is not sufficient for use in HK because the bigger size of tank than SK will increase the path of light and the light attenuation. Additionally, HK aims to increase the sensitivity of targeted physics, for example low energy physics like supernova relic neutrino or proton decay especially for  $p \rightarrow \bar{\nu}K^+$  mode and the newly developed reconstruction algorithm like neutron tagging compared to SK. Moreover, high performance photodetectors extend the possibility to develop new analysis methods. Therefore, it is necessary to develop new higher performance photodetectors than SK PMT.

The requirements for photodetectors are summarized in Table 2.1. They are determined by the physics sensitivity aimed in HK. The value of each requirement is evaluated based on the performance of SK and SK PMTs.

Better charge resolution is necessary for better energy resolution. Especially for detecting a low energy particle, because several photons are yields and each photodetector detects one photon, the single photon counting performance becomes important.

Better timing resolution is required for better vertex reconstruction. The interaction vertices of particles are reconstructed in water by the shape of Cherenkov image and the timing information of Cherenkov light detected in each photodetectors. Less timing jitter makes better reconstruction performance.

Low dark rate is important for suppressing the background of low energy

event and the amount of DAQ data. Afterpulse also becomes the background of delayed particle like Michel electron and contribute to the increase of dark rate. It is desirable to reduce afterpulse.

Rate tolerance is important to measure supernova explosions. In HK,  $O(10^5)$  Hz event rate in low energy is expected if supernova explosion occurs at 10 kpc from the earth. Therefore, it is necessary for the photodetectors to have sufficient rate tolerance.

Higher detection efficiency is needed because the tank size of HK becomes bigger than SK and the attenuation of light increase. Detection efficiency becomes important especially for detecting a low light event. On the other hand, wide dynamic range is essential to observe a high energy event which yields numerous number of photons.

The mechanical robustness of photodetectors is also required. In order to reduce the influence of terrestrial magnetism, photodetectors must have magnetic field tolerance. Low failure rate and long lifetime is necessary because photodetectors will be operate in water for 20 years in HK. The high water pressure tolerance is needed because the depth of HK tank is 80 m while that of SK is 40 m.

Table 2.1: Minimum requirements for the Hyper-K inner photodetectors, based on the performance of SK PMT(R3600) and HK.

Requirements	Value	Conditions
Gain	$10^7 \sim 10^8$	Typ.
Signal window	200 ns	Max. More than 95% of a total signal area
Charge resolution	50%	Typ. $\sigma$ of p.e.
Timing resolution	2.4 ns	Typ. FWHM of single photoelectron (p.e.) <sup>1</sup>
Dark rate	4 kHz	Typ. For 1/4 p.e. threshold
Afterpulse rate	15%	Max. For single p.e. , relative to the main pulse
Rate tolerance	10 MHz	Max. single p.e. pulse, within 10% change of gain
Detection efficiency	16%	Typ. Quantum efficiency $\times$ Collection efficiency
Dynamic range	2 photons/cm <sup>2</sup>	Max. Per detection area on wall
Magnetic field tolerance	100 mG	Typ. Within 10% degradation
Lifetime	20 years	Typ. Less than 10% dead rate
Pressure rating	0.8 MPa	Max. Static, load in water

<sup>1</sup>The original requirement uses  $\sigma$  of single photoelectron (p.e. ), but in this thesis we use FWHM because the transit time distribution is not gaussian but asymmetrical distribution.

## 2.2 Photodetector candidates for Hyper-K

### 2.2.1 Box&Line PMT

In SK, 50 cm venetian blind PMT (Hamamatsu R3600 NQE (normal QE), called Super-Kamiokande PMT (SK PMT)) is used as a photodetector for 20 years. Fig. 2.1 shows the structure of SK PMT. SK PMT uses the venetian blind structure as dynodes and it allows to increase the size of photocathode easily. However, there is a room to improve the performance. Fig. 2.2 shows the performance of SK PMT. Multiple photo-electron paths due to the structure of venetian blind dynodes worsen its timing resolution, and a low probability to hit the first stage of dynodes results in worse charge resolution and detection efficiency.

In order to improve the performance of the photodetector, Box&Line PMT (B&L PMT) is newly developed as a successor of SK PMT for use in HK. A B&L PMT has the large first dynode of box shape and dynodes of line shape for the rest. As shown in Fig. 2.2, box dynode maintain high collection efficiency and line dynodes make uniform path length of photoelectrons. It is result in a good timing and charge resolution as shown in Fig. 2.2.

When the performance evaluation of HPD, the main theme of this thesis, it becomes important to compare with the performance of these SK PMT and B&L PMT.

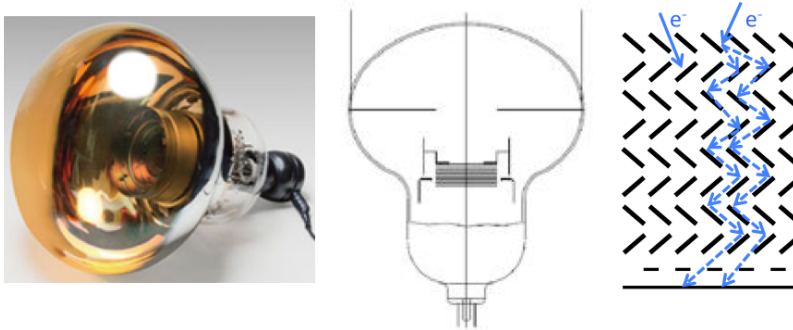


Figure 2.1: Venetian blind PMT / Super-Kamiokande PMT (SK PMT) / Hamamatsu R3600 NQE.

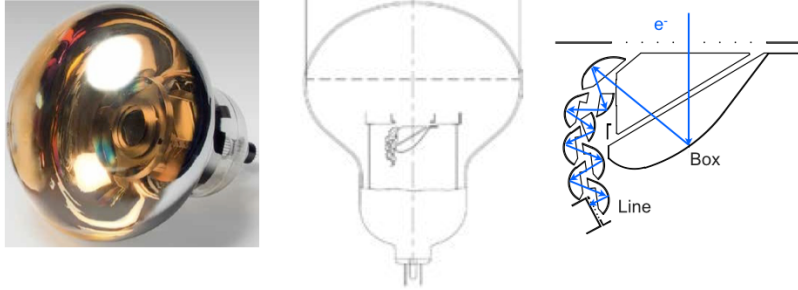


Figure 2.2: Box&Line PMT (B&L PMT) / Hamamatsu R12860 HQE.

Table 2.2: The performance summary of SK PMT and B&L PMT.

	SK PMT	B&L PMT
Rise Time [ns]	10.6	7.6
Fall Time [ns]	13.2	16.0
FWHM [ns]	18.8	12.2
Charge resolution [%]	53	35
Timing resolution (TTS in FWHM) [ns]	7.0	4.0

### 2.2.2 Hybrid Photo-Detector

A Hybrid Photo-Detector is a photodetector using a silicon avalanche diode instead of metal dynodes which are used in a PMT. Fig. 2.3 shows the method of a signal amplification in an HPD. First, photo-electrons produced at the photocathode are accelerated towards the AD by a high voltage electric field ( $\sim 8$  kV), result in multiplication by bombardment. Second, electron-hole pairs are created inside the AD, where a bias voltage of  $400\sim 500$  V is applied to amplify electrons by a factor of  $\sim 50$  in avalanche multiplication. The gain of an HPD alone becomes  $\sim 10^5$  and a preamplifier is employed to obtain the total gain equivalent to a SK PMT ( $\sim 10^7$ ).

It is expected that an HPD would have many advantages compared to a PMT. An HPD has better charge resolution because of the high gain at the first amplification stage, and due to its small fluctuation of the drift path in the AD the timing resolution of a HPD is better. The simpler and axial symmetric structure makes lower costs, better magnetic field tolerance and lower afterpulse.

Fig. 2.4 shows the history of the development of HPDs. First, as a prototype of a large aperture HPD, a 20 cm HPD with a 5 mm diameter ( $\phi$ ) AD was developed [20]. The prototypes are now under a proof test in a 200 ton water tank where they showed good performances [21]. In order to test the production of large photocathode HPD, a 50 cm HPD with 5 mm  $\phi$  AD is developed as a simple extended version of 20 cm HPD with 5 mm  $\phi$  AD. While it is confirmed

that it has good performances as well [22], the collection efficiency is low. To improve collection efficiency (CE), the large area of AD is necessary. According to the simulation result from Hamamatsu, a 20 mm AD can reach to CE $\sim$ 93% while a 5 mm AD reach to  $\sim$ 10%. Therefore, a 50 cm HPD with 20 mm  $\phi$  AD becomes our target design. However, it is accompanied with a large noise by a large 800 pF junction capacitance, increased from 50 pF in the 5 mm  $\phi$  AD. This is described in detail in next section.

### 2.2.3 Goals of this thesis

In this thesis, we report R&D of a 50 cm HPD which can be used as inner photodetector of HK. To increase a collection efficiency of a 50 cm diameter HPD, a large area AD is necessary, but a large junction capacitance of a large area of AD increases the noise level of the output signal as explained in Section 3.1. We developed new AD (Section 3.2) and preamplifiers (Section 3.3) to solve this problem and succeed to separate single photoelectron signal and baseline noise.

Then we evaluate the performance of a 50 cm HPD. We describe the result of evaluation in Section 4.

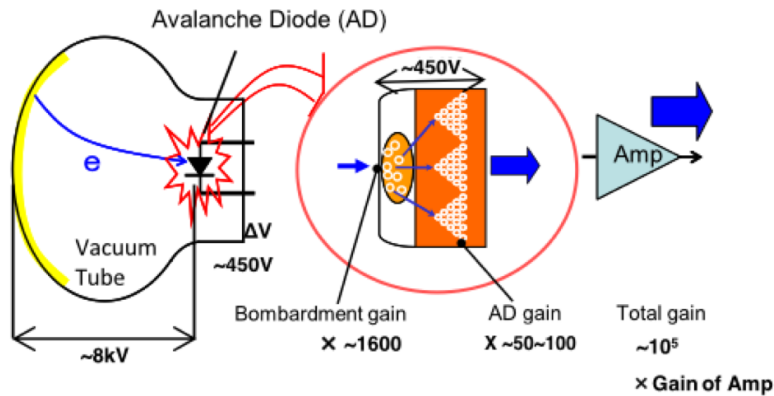


Figure 2.3: The principle of an HPD amplification and typical values of the 50cm HPD.

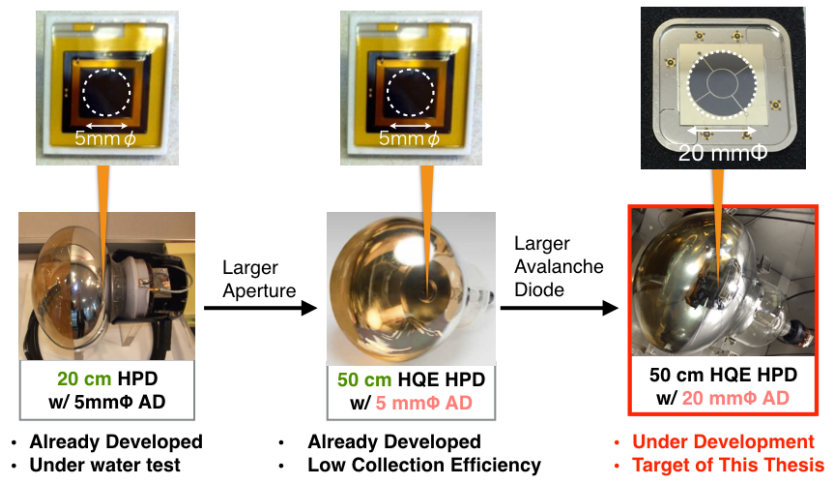


Figure 2.4: Summary of HPD development.

## Chapter 3

# Development of 50 cm HPD with 20 mm diameter avalanche diode

### 3.1 Difficulty of using 20 mm diameter AD

To increase the collection efficiency (CE) of a 50 cm diameter HPD, a large area AD is necessary. We developed a 50 cm diameter HPD with a 20 mm diameter AD based on a 50 cm diameter HPD with a 5 mm diameter AD. However, a large junction capacitance of a large area of AD increases the noise level of the output signal [23].

Fig. 3.1 shows the principle of the noise increase due to a large junction capacitance of an AD and a trans-impedance amplifier (a current-to-voltage converter). If the feedback impedance is fixed and the input capacitance of preamplifier  $C = C_d C_i / (C_d + C_i)$  increases, the input impedance decreases by  $1/\omega C$  and the noise of preamplifier increases. Then, a current noise is amplified by a feedback and the signal to noise ratio (S/N) becomes worse. In current situation,  $C_d$  is much larger than  $C_i$ , therefore it is necessary to decrease the junction capacitance of an AD.

To solve this problem, following improvements are attempted:

- AD improvement
  - Development of new AD with low capacitance
  - Development of segmented (or multichannel) AD
- Preamplifier improvement
  - Tuning parameters of trans-impedance amplifier
  - Introduction of decoupling transformer

- Bootstrap circuit
- Non-feedback amplifier

In this thesis, new AD with low capacitance, segmented (or multi-channel) AD and tuning parameters of trans-impedance amplifier are applied. In the following sections, we describe them in detail. Other improvements are also evaluated. For example, the application of decoupling transformer is tried in [24].

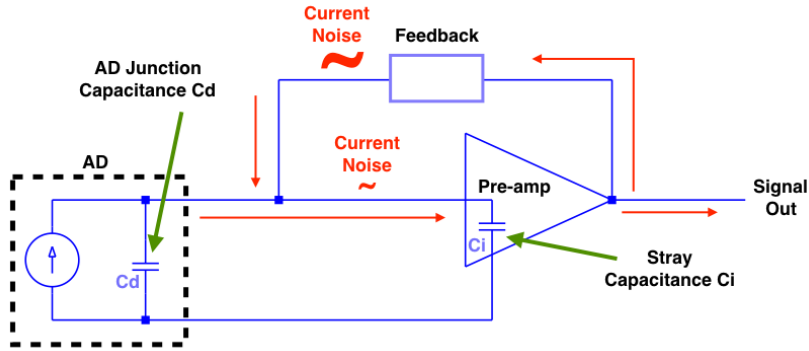


Figure 3.1: The principle of current noise increase due to the large junction capacitance of an AD and a trans-impedance amplifier.

## 3.2 Improvement of AD

### 3.2.1 Development of low capacitance AD

The development of new AD with low capacitance is achieved by increasing the thickness of an AD. The junction capacitance of the original AD is 800 pF and that of a new AD is reduced by half (400 pF). The bias voltage of a new low capacitance AD increases compared to the original AD in order to obtain the same gain. Accordingly, the coupling capacitance inside the base block and a guard voltage are changed. The typical values of each type of AD are summarized in Table 3.1.

### 3.2.2 Application of segmented AD

By dividing an AD into multiple channels, we can reduce the junction capacitance per channel. We have developed two types of segmented ADs: 5ch AD and 2ch AD. A 5ch AD has one circular AD at the center and four surrounding arc-like ADs. A 2ch AD has one large circular AD at the center and one surrounding doughnut-like AD. Each channel is designed to have the same area so that the junction capacitance becomes equal for all channels. Currently, the

AD cathode is common between channels. In the future, the AD cathode will be also separated into each channels.

Fig. 3.2 shows a schematic view of a segmented AD and its readout system. The signal of each channel of an AD is amplified by a preamplifier. There are two method of the final read-out of signal output. One is to read out each channel of an AD individually. We have the signal outputs with the same number of segmentations and each signal is amplified by a preamplifier. Second is to read out by using a sum-amplifier with one signal outputs. The individual read-out scheme can suppress the noise at the price of increased number of channels. On the other hand, the sum-amp read-out scheme has less number of channels but larger noise. The total noise level of sum-amp read-out becomes  $\sqrt{\sum(\text{noise from each channel})^2}$ .

Fig. 3.3 shows the AD junction capacitance dependency of the noise level of the output signal in pulse height and in standard deviation of charge. We measure the output signal of a raw AD by connecting each channel of 5ch old AD or 5ch low capacitance AD in parallel and varying the value of a junction capacitance. The noise level of an HPD with 5ch old AD is also measured in order to confirm the consistency between the measurements using AD alone or an HPD equipped with an AD. It is confirmed that the noise level of an HPD output signal is suppressed by reducing the AD capacitance.

Table 3.1: Summary of AD types and typical values. 1ch AD means not-segmented AD.

Number of Segment [ch]	Thickness of AD	Total Capacitance [pF]	Capacitance of Each Channel [pF/ch]	Bias Voltage [V]
5	thin	800	160	~400
5	thick	400	80	~500
2	thin	800	400	~400
2	thick	400	200	~500
1	thin	800	800	~400
1	thick	400	400	~500

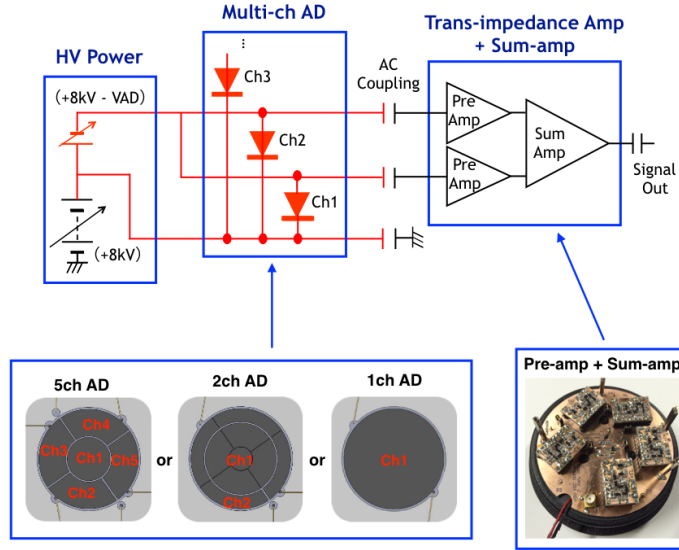


Figure 3.2: Schematic view of segmented AD and readout system.

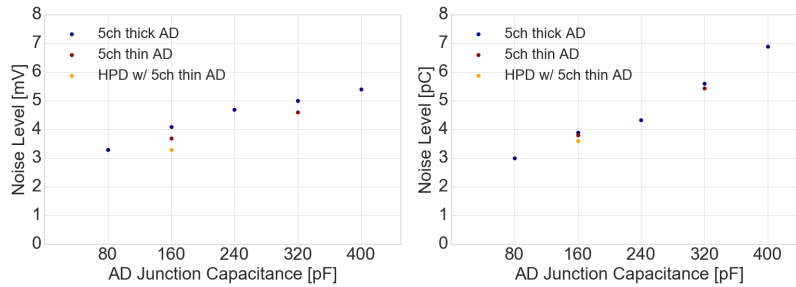


Figure 3.3: The AD junction capacitance dependency of the noise level in pulse height (left) and in charge (right).

### 3.3 Improvement of preamplifier

#### 3.3.1 Difficulties in preamplifier development

There are three issues in the development of a preamplifier for a 50 cm HPD with a large diameter AD as shown in Fig. 3.4. First is the large junction capacitance as described in previous sections. It increases the output noise and worsen S/N. Second is the floating current source due to the high voltage between an AD

and ground. Because of first and second reasons, we cannot use the preexisting preamplifier and have to develop new one. Third is the non-negligible delay line between an AD and a preamplifier which generates the phase rotation in high frequency. In the development, we mainly try to solve first and second problems and third one had not been recognized until August 2016. As described later section, the development of a preamplifier is accomplished by solving third one.

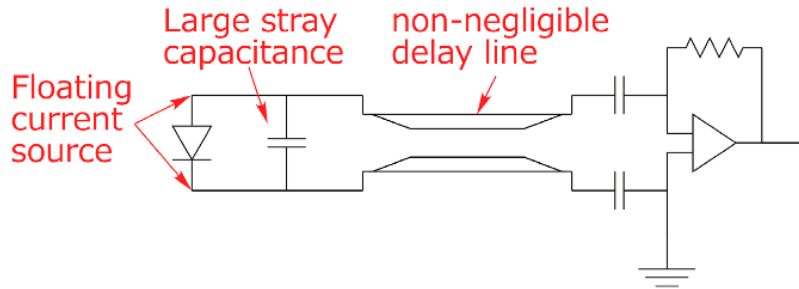


Figure 3.4: Description of problems to develop the preamplifier of 50 cm HPD with 20 mm diameter AD.

### 3.3.2 Sequence of preamplifier development

The development of a preamplifier is carried out as follows.

First, a preamplifier is made at ICRR, the University of Tokyo or Hamamatsu photonics and pre-tested. Fig. 3.5 shows the test board of a preamplifier used in ICRR. To simulate the structure of an HPD, differential inputs and a capacitor are equipped. A square wave and inverted one enter the two inputs and 8fC charge is generated, which is equivalent of the raw output of an HPD. The capacitor is exchangeable and we can test with various size of capacitors.

After the pre-test and clear  $S/N$  (= pulse height of signal / root mean square(RMS) of baseline noise level.)  $> 10\sigma$ , we evaluate the performance of a preamplifier using an HPD at Kamioka or Kashiwa. We check that there no oscillation, whether 1 p.e. signal can be triggered by 0.25 p.e. threshold and whether 1p.e. signal can be separated in charge distribution.

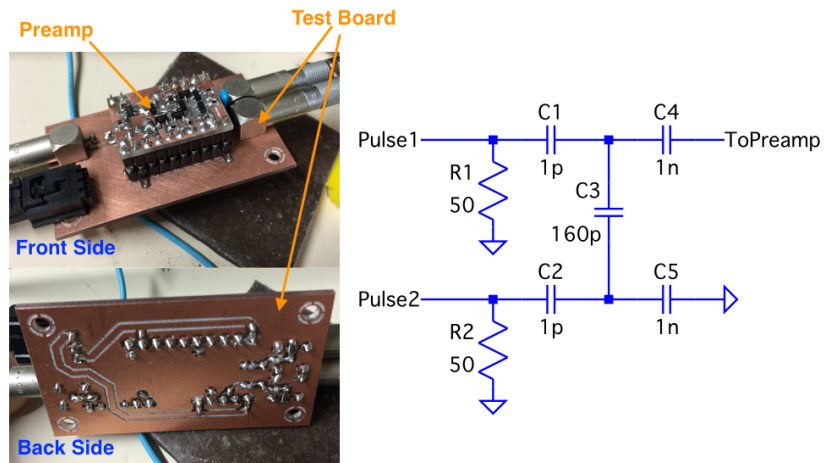


Figure 3.5: Left (right) is the image (circuit diagram) of the preamplifier test board.

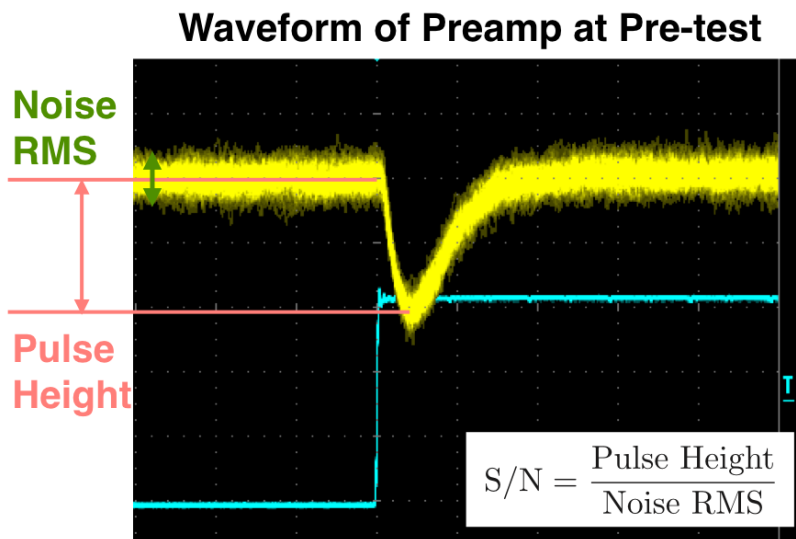


Figure 3.6: The output signal waveform of a preamplifier at the pre-test.

### 3.3.3 Developed preamplifiers

In this section, we overview the developed preamplifiers. We can divide preamplifiers into three types by developed period and its characteristic (summarized in Table 3.3).

First type is simple transplantation of a trans-impedance preamplifier used for an HPD with 5 mm diameter AD. Its parameters are tuned for an HPD with 20 mm diameter AD, but the S/N is low and there are large ringings.

Second type is developed in January 2016. It increases the feedback of the preamplifier and strengthen its ground to suppress the overshoot of the output signal and noise level. Fig. 3.7 shows the comparison of waveform and charge distribution between type I and II preamplifiers. Type II had better S/N, but the rise time becomes long and the gain becomes large. Despite of its slow response, we can detect a single photo-electron signal, so we used this type of preamplifier for the performance evaluation of charge resolution, dark rate, afterpulse and rate tolerance.

Third type is developed to solve the third problem described in Section 3.3.1. It decreases the open loop gain of preamplifier especially in high frequency region and improves S/N and signal response. This type of preamplifier is the final version and used in the evaluation of timing resolution. Fig. 3.8, 3.9 compare the output signal waveform and charge distribution of type II and III preamplifiers. The rise time of type III is faster than type II keeping the same charge resolution.

## 3.4 Summary of developed HPD types

Following the solutions described in previous sections, we have developed three types of HPDs: HPD with 5ch AD (160 pF/ch), HPD with 2ch half capacitance AD (200 pF/ch), HPD with 1ch half capacitance AD (400 pF/ch). Fig. 3.2 shows the usage of each type.

Table 3.2: Summary of HPD types and evaluation using each type of HPD.

Serial No.	Type	Usage
THD0034	HPD with 5ch high capacitance AD	1 p.e. resolution, position sensitivity
THD0056	HPD with 2ch low capacitance	1 p.e. resolution, dark rate, rate tolerance
THD0058	HPD with 1ch low capacitance	1 p.e. resolution, dark rate, afterpulse, detection efficiency
THD0061	waterproof HPD with 1ch low capacitance	waterproof test

Table 3.3: Summary of developed preamplifiers.

Type	Developed Period	Characteristic
I	2015	low S/N, large ringing
II	the beginning of 2016	high S/N, small ringing, long rise time
III	August 2016	high S/N, small ringing, short rise time

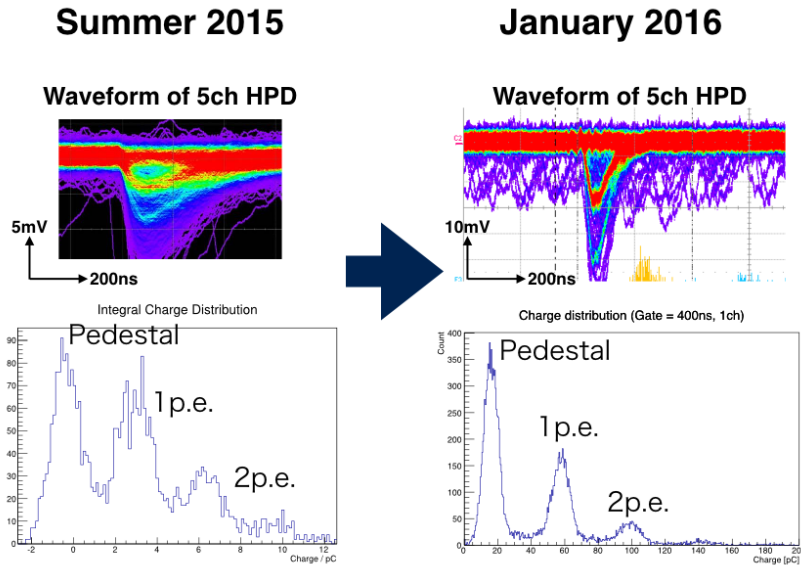


Figure 3.7: Comparison of waveform and charge distribution between type I and II preamplifier.

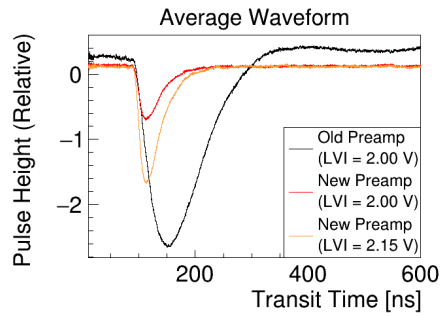


Figure 3.8: The comparison of old and new preamp in waveform.

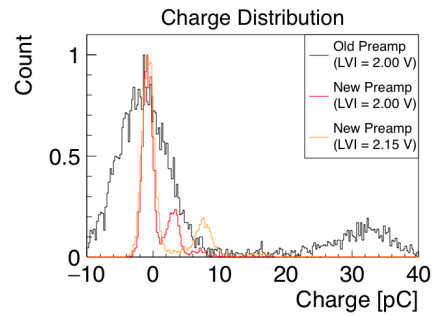
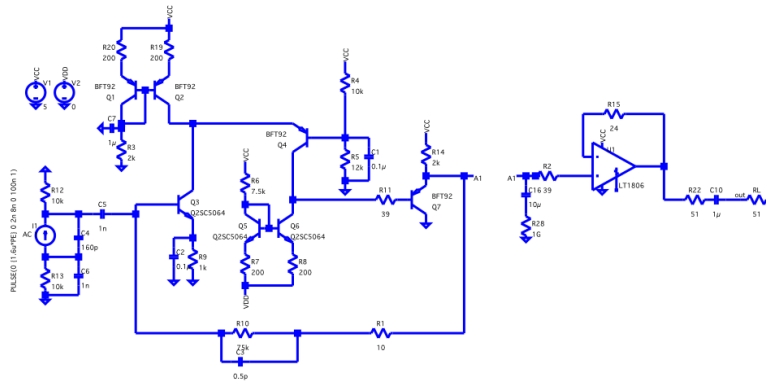


Figure 3.9: The comparison of old and new preamp in charge distribution.



10

Figure 3.10: Circuit diagram of type I preamplifier.

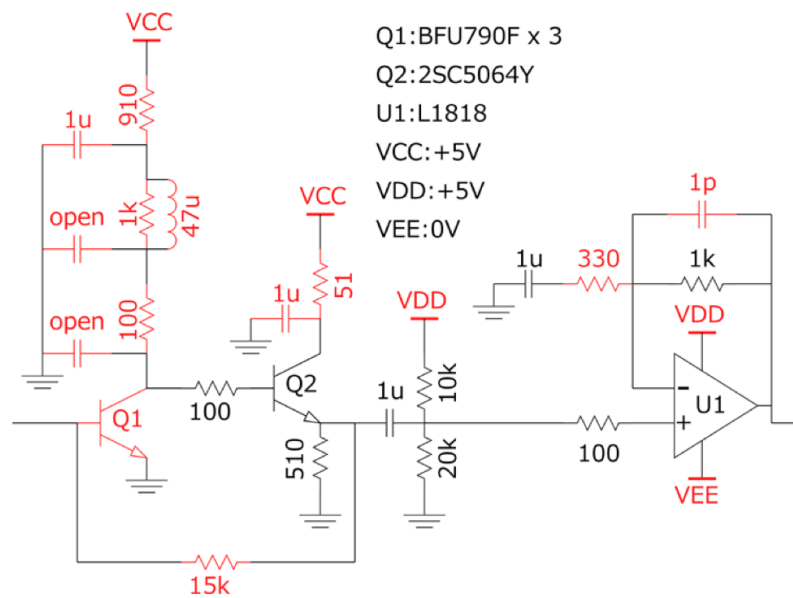


Figure 3.11: Circuit diagram of type II preamplifier.

## Chapter 4

# Performance evaluation of 50 cm HPD

### 4.1 Setup for performance evaluation

Fig. 4.1 shows the overview of the whole system to operate an HPD and collect data. An HPD is located in a dark box. Photons are emitted from the pico pulse laser and sent to the HPD via an optical fiber. The signal is read-out from the cable derived from the socket assembly of an HPD and processed by a DAQ system depending on each measurement.

An HPD designed for R&D can be divided into two parts. One is the glass bulb with a photocathode and an AD. The other is the socket assembly consisted of a HV module, a base-block and preamplifier(s) (+ sum-amp) as shown in Fig. 4.2. The HV module is used to apply two kinds of voltage, the one between the photocathode and the AD (typically  $\sim 8$  kV), and the bias voltage of AD (400 $\sim$ 500 V). The output of HV module is controlled by an external HV-LV control power supply shown in Fig. 4.3. In the base-block, decoupling capacitors are built-in to transmit the high voltage from the HV module to the HPD, and read-out the raw signal of the HPD. The preamplifier amplifies the raw signal of HPD. If an HPD has a segmented AD, additional preamplifiers and sum-amplifier are implemented. The socket assembly is detachable mainly in order to test preamplifiers. In the final version of an HPD, the parts of socket assembly and glass bulb will be united.

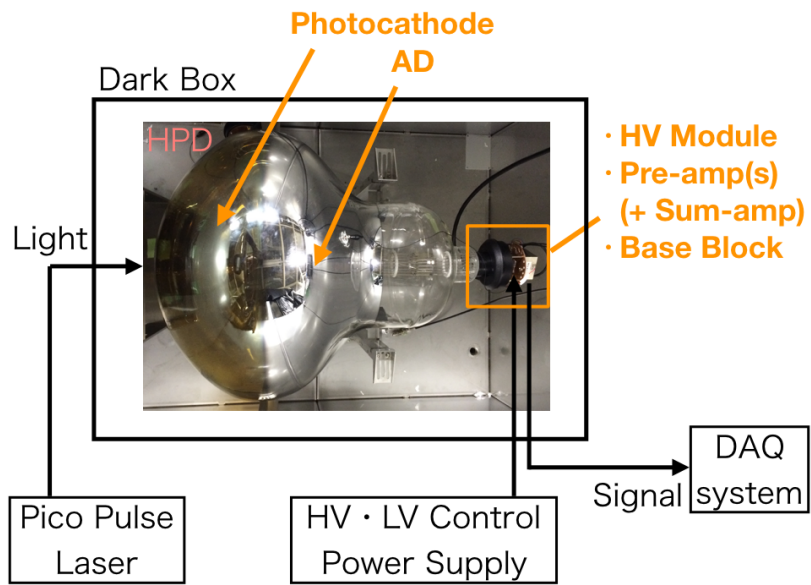


Figure 4.1: The overview of the whole system to operate an HPD and data acquisition.

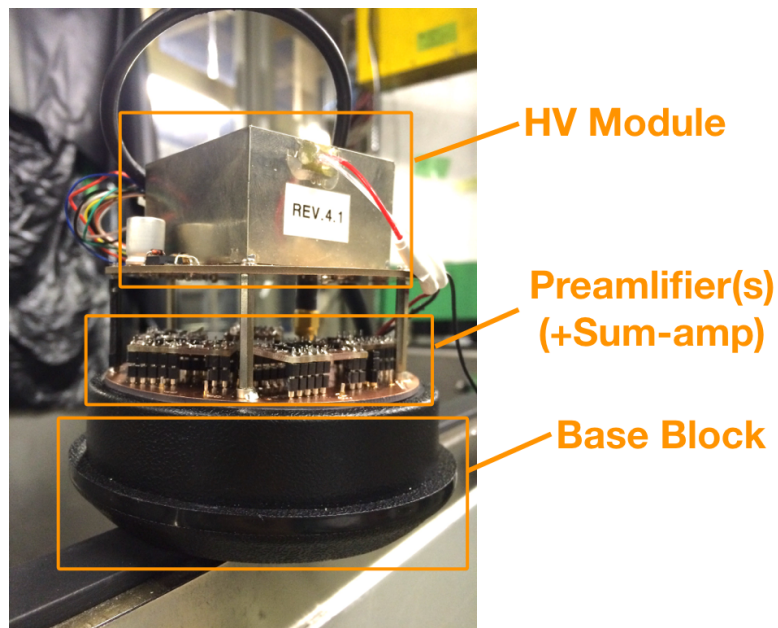


Figure 4.2: A picture of the socket assembly of HPD.

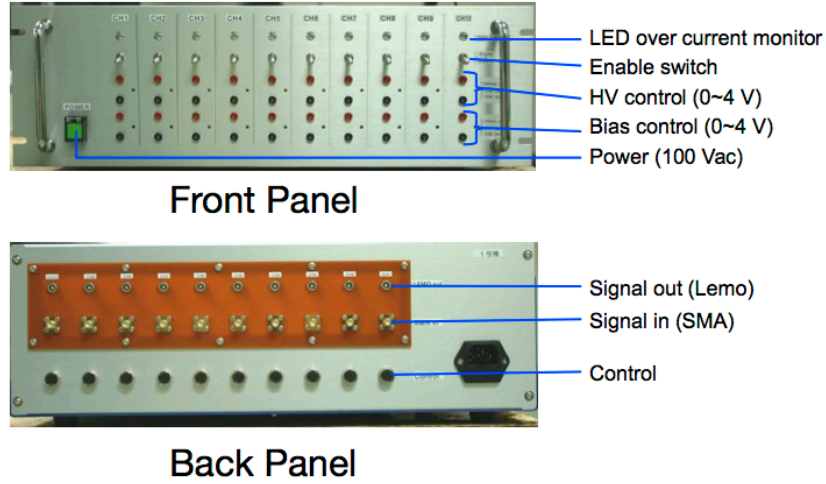


Figure 4.3: Pictures of the HV-LV control power supply.

## 4.2 Waveform

Fig. 4.4 shows each photodetector's waveform normalized by its pulse height. Table 4.1 shows the rise time, fall time and FWHM of each photodetector. Rise time (fall time) is defined as the time required for the response to rise (fall) from 10% (90%) to 90% (10%) of the maximum pulse height. The intrinsic HPD (which means HPD without preamplifier) has the best rise time compared to SK PMT or B&L PMT and less ringing. While the response of HPD with the old preamp becomes slower than others, new preamp succeeds to bring out the potential of HPD.

Table 4.1: Summary of rise time, fall time and FWHM of each photodetector.

PD Type	Rise Time [ns]	Fall Time [ns]	FWHM [ns]
HPD (with old preamp)	37.2	111.9	107.2
HPD (with new preamp)	13.4	59.2	41.3
HPD (without preamp)	6.3	47.7	28.7
SK PMT	10.6	13.2	18.8
B&L PMT	7.6	16.0	12.2

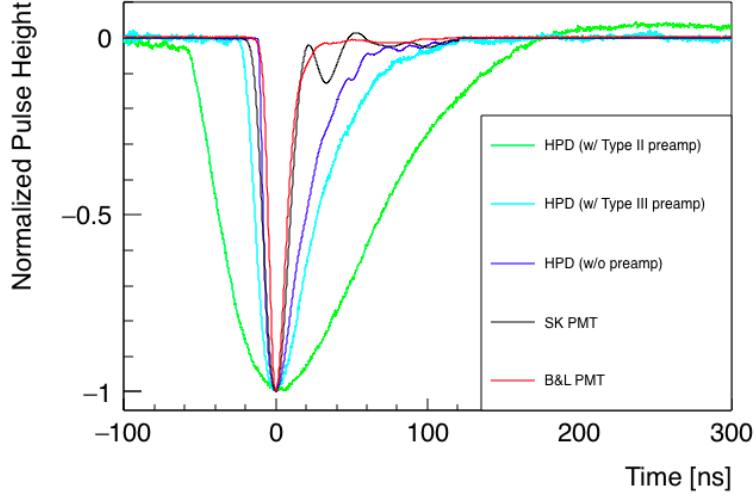


Figure 4.4: Waveform of each photodetector.

### 4.3 Gain

The gain of photodetector is defined as the output charge of 1 p.e. signal divided by the elementary charge. The gain of HPD is proportional to HV as shown in Fig. 4.5 and depends on the AD bias voltage with the following function:

$$\text{gain} = \frac{a}{1 - (\text{Bias}/b)^c} \quad (4.1)$$

as shown in Fig. 4.6. The gain of HPD also depends on the temperature because the AD gain increases as the temperature decreases with the same AD bias voltage.

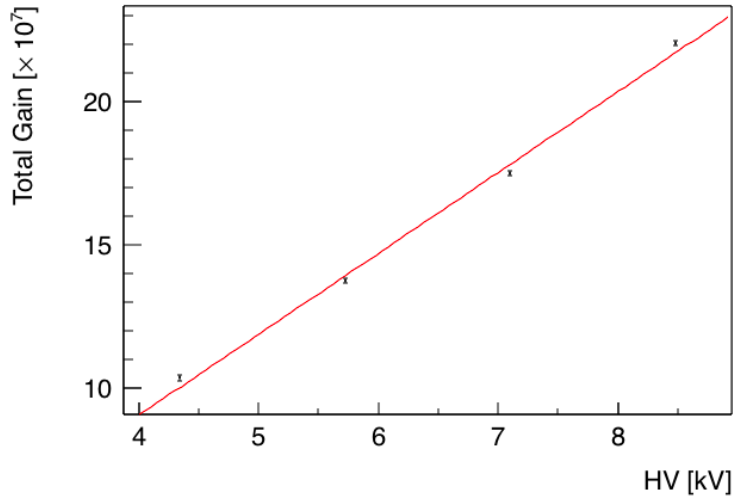


Figure 4.5: Measured total gain of 1ch HPD with preamplifier as a function of the HV with fixed AD bias voltage of 520 kV.

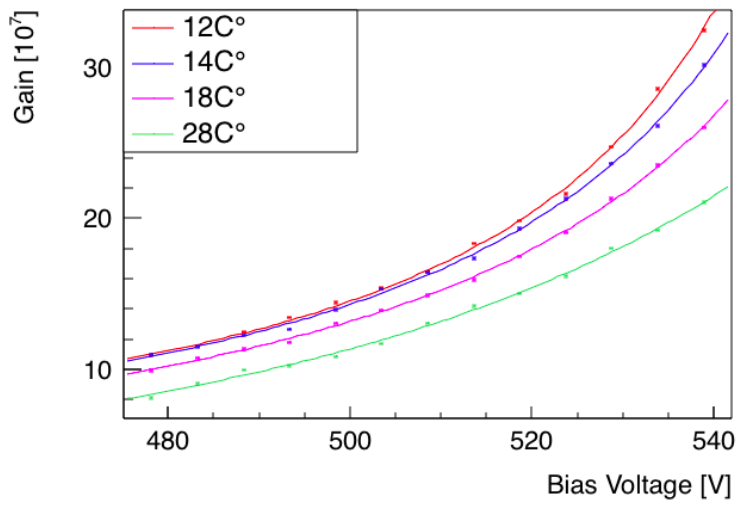


Figure 4.6: Measured total gain of 1ch HPD with preamplifier as a function of the AD bias voltage with fixed HV of 8 kV.

## 4.4 Charge resolution

We measure the 1 p.e. charge distribution of 5ch, 2ch or 1ch HPD by ADC with the gate width is 200 ns. Fig. 4.7 shows the result of single channel and sum-amp readout. The detection capability of single photo-electron (p.e.) is evaluated by calculating 1 p.e. resolution, noise level, peak to valley ratio (P/V) defined as

$$1 \text{ p.e. resolution} = \frac{\sigma_{1 \text{ p.e.}}}{\mu_{1 \text{ p.e.}} - \mu_{\text{ped}}} \quad (4.2)$$

$$\text{noise level} = \frac{\sigma_{\text{ped}}}{\mu_{1 \text{ p.e.}} - \mu_{\text{ped}}} \quad (4.3)$$

$$\text{peak to valley ratio (P/V)} = \frac{\text{Peak}}{\text{Valley}} \quad (4.4)$$

where  $\mu_{1 \text{ p.e.}}$ ,  $\mu_{\text{ped}}$ ,  $\sigma_{1 \text{ p.e.}}$ ,  $\sigma_{\text{ped}}$ , peak and valley are evaluated by fitting charge distribution by a composite function of two Gaussian and two error functions as shown in Fig. 4.8. The error functions are used to take into account the contamination of photo-electron backscattering on the AD which forms the flat regions between pedestal and 1p.e. or 1p.e. and 2p.e. peaks. Table 4.2 shows the summary of evaluated 1 p.e. resolution, noise level, peak to valley ratio of each photodetector.

Single channel readout of 5ch HPD or 2ch HPD has three times better 1 p.e. resolution than B&L PMT or SK PMT. Sum-amp readout of 5ch HPD has worse 1 p.e. resolution and noise level because of common mode noise, however sum-amp readout of 2ch HPD and single channel readout of 1ch HPD has still twice better 1 p.e. resolution than B&L PMT or SK PMT.

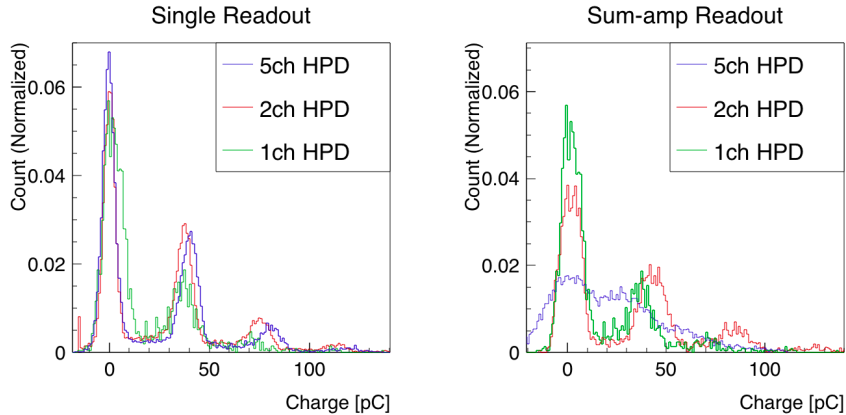


Figure 4.7: 1 p.e. charge distribution of 5ch, 2ch, 1ch HPD by single channel readout (left) and sum-amp readout (right).

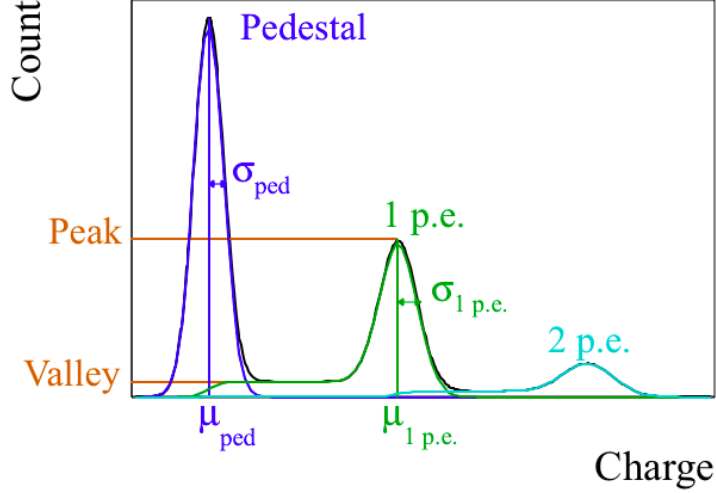


Figure 4.8: Definition of  $\mu_{1 \text{ p.e.}}$ ,  $\mu_{\text{ped}}$ ,  $\sigma_{1 \text{ p.e.}}$ ,  $\sigma_{\text{ped}}$ , peak, valley in charge distribution.

Table 4.2: Summary of 1 p.e. resolution, noise level, peak to valley ratio of each photodetector.

PD Type	1 p.e. resolution [%]	noise level [%]	P/V
5ch HPD (Single)	10.0	7.9	10.1
5ch HPD (Sum)	36.6	40.2	1.1
2ch HPD (Single)	10.3	7.6	8.4
2ch HPD (Sum)	14.8	11.1	8.9
1ch HPD	17.7	13.8	7.3
B&L PMT [25]	35	-	4.8
SK PMT [25]	53	-	1.9

## 4.5 Timing resolution

The timing resolution of HPD is evaluated by measuring the transit time spread (TTS), which is defined by the time from a trigger of a light source to 0.5 p.e. threshold as shown in Fig. 4.9.

Fig. 4.11 shows the setup for the measurement of the timing resolution. The pico-pulse laser is triggered by the input/output (I/O) resistor and the light intensity is controlled by an attenuator. The output signal of the HPD is divided and measured by an ADC and a TDC. The gate triggers of the ADC and the TDC are synchronized by I/O resistor and we can measure the charge and transit time of the HPD simultaneously.

Fig. 4.10 is the result of the single photoelectron TTS measurement. The 1 p.e. TTS of each photodetector after applying time walk correction are overwritten. The evaluated TTS in FWHM is summarized in Table 4.3. The TTS of 1ch HPD becomes 3.3 ns with bias voltage of 520 V and 2.7 ns with bias voltage of 570 V after time walk correction. This is twice better than that of SK PMT and better than that of B&L PMT.

We also measure the TTS for multiple p.e. signal of HPD. Fig. 4.12 shows the measured TQ-map (the relation between charge and timing) of 1ch HPD and Fig. 4.13 is the evaluated TTS in FWHM with time walk correction for each number of photoelectrons. It is shown that the TTS of HPD is better than that of SK PMT and B&L PMT especially for multiple p.e. signal<sup>1</sup>.

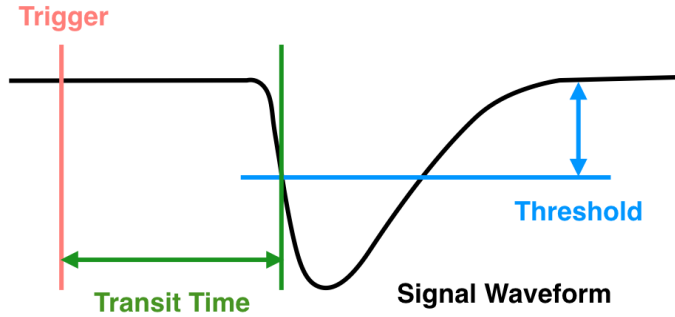


Figure 4.9: Definition of transit time.

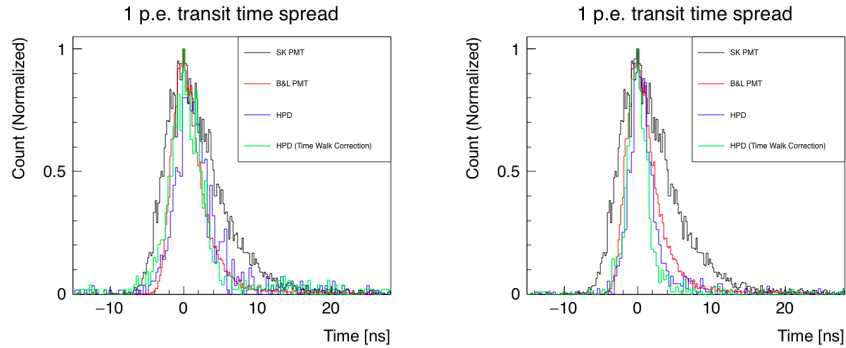


Figure 4.10: Single photo-electron transit time spread (TTS) of each photodetectors. Left (right) figure contains TTS of HPD with the bias voltage  $\sim 520$  V ( $\sim 570$  V).

<sup>1</sup>The 1 p.e. TTS of HPD in Fig. 4.13 becomes worse than that in Fig. 4.10 because the used preamplifier is different (the circuit structure is the same but the components is different) and the time walk correction using TQ-map has less impact on small p.e. signals than large p.e. signals

Table 4.3: The summary of single photoelectron timing resolution for each photodetectors.

PD Type	Conditions	TTS(FWHM) [ns]	TTS(FWHM, time walk correction) [ns]
SK PMT	-	-	7.0
B&L PMT	-	-	4.0
1ch HPD	Bias $\sim$ 520 V	4.0	3.3
1ch HPD	Bias $\sim$ 570 V	3.0	2.7

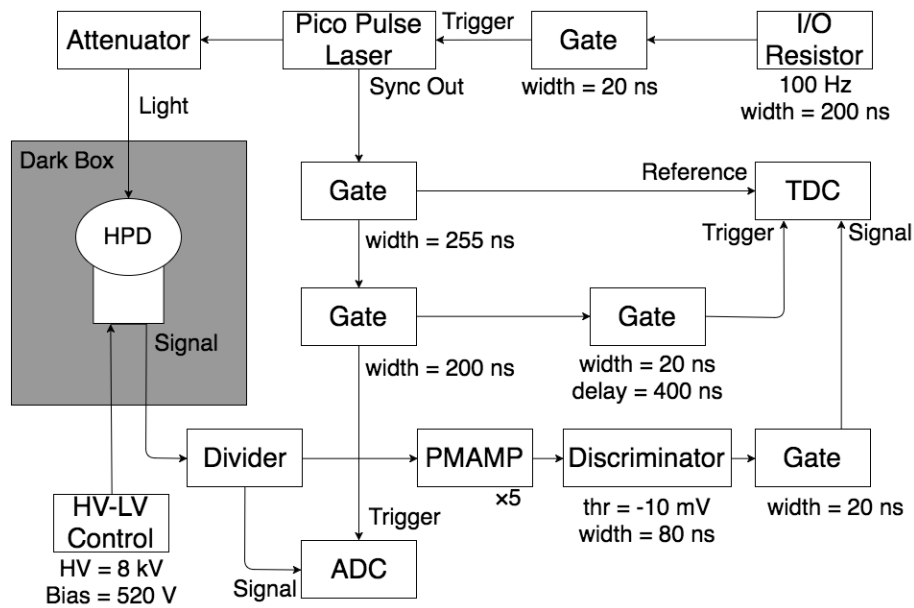


Figure 4.11: Setup of the timing resolution measurement.

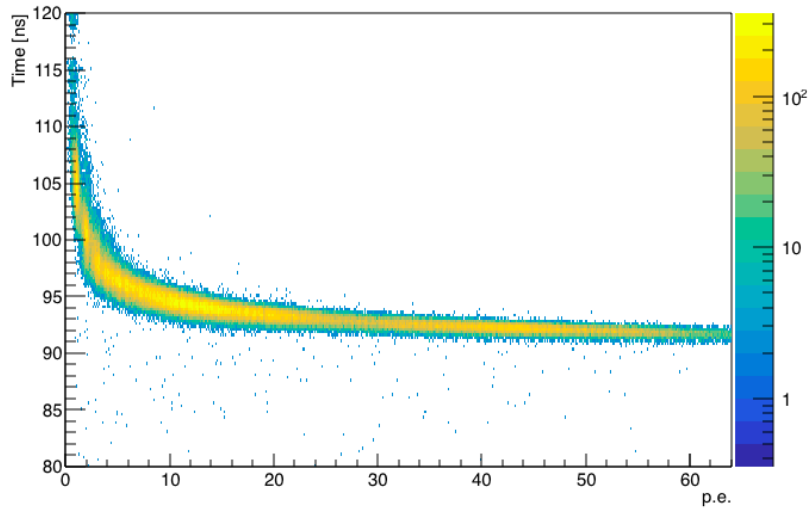


Figure 4.12: The TQ-map (time charge map) of 1ch HPD.

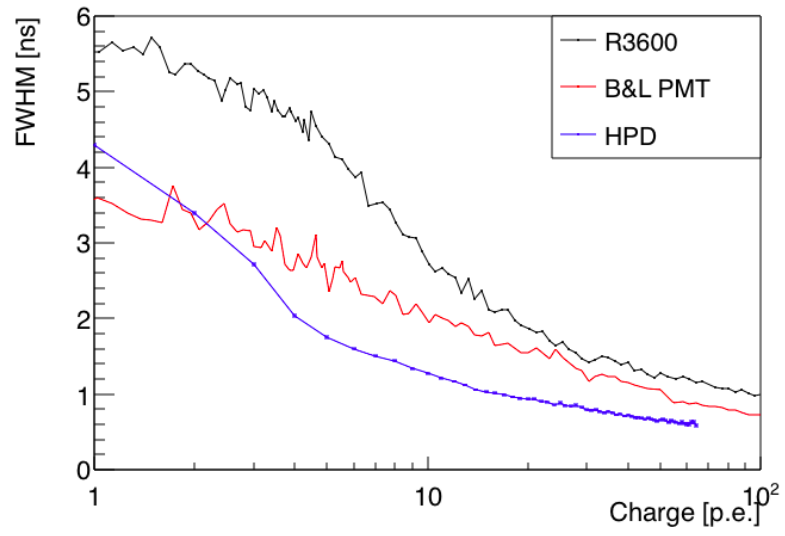


Figure 4.13: Multi photo-electron transit time spread (TTS) of each photodetectors.

## 4.6 Dark rate

Dark count rate is the signal pulse rate of photodetectors without light input. The dark pulse of HPD is caused by the thermal electron emissions from the photocathode and mainly observed as 1 p.e. signal.

We measure the dark rate of HPD as a function of the threshold after keeping it in a dark box for a few days with applying high voltage and bias voltage at room temperature (25°C). We use an Analog Timing Module (ATM) board, a DAQ board used in Super-K I, II and III. A detailed description for ATM can be found in Ref. [26]. The threshold of ATM can be set from 0 mV to 12.5 mV. Because the pulse height of the signal of HPD is  $\sim 15$  mV, we use divider to make the height in half.

Fig. 4.14 shows the measured dark rate of 1ch HPD and 2ch HPD. The dark rate of HPD is  $\sim 10$  kHz with a threshold of 0.5 p.e. Considering the temperature dependence, the dark rate of HPD is expected to be the same level as that of SK PMT ( $\sim 4$  kHz) at water temperature ( $\sim 16^\circ\text{C}$ ) in HK operation from the dark rate measurement of a 50 cm HPD with 5mm diameter [24] or that of a waterproof 50 cm HPD in Section 4.10. It is still not stabilized completely and there might be room to reduce the level further.

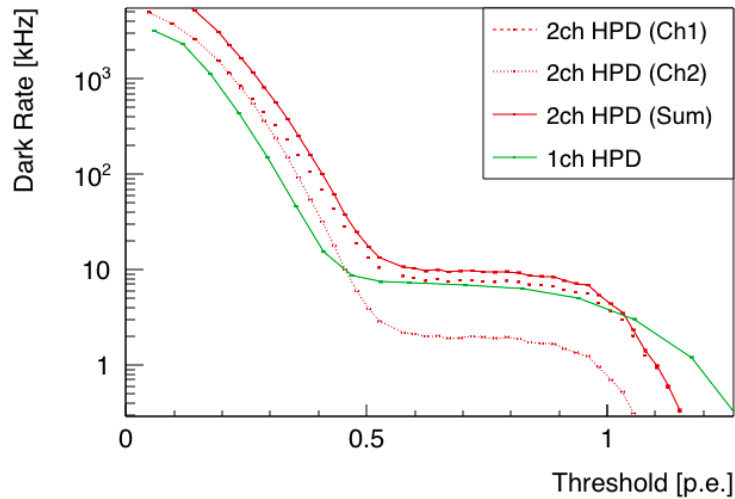


Figure 4.14: The dark rate of 1ch and 2ch HPD as a function of the threshold. The dotted red line shows the dark rate of each channel of 2ch HPD and the solid red line shows the sum of two dotted red lines.

## 4.7 Photon detection efficiency

We cannot measure the collection efficiency of photodetectors directly, so we measure the total detection efficiency, which is equal to collection efficiency (CE)  $\times$  quantum efficiency (QE), relatively by comparing with reference PMTs.

Fig. 4.15 shows measured relative total detection efficiency, QE measured by Hamamatsu photonics and calculated relative CE. The total detection efficiency of HPD is the same level of that of B&L PMT, while the CE of HPD is lower than B&L PMT.

This is because the trigger efficiency of HPD is low as shown in Fig. 4.16. The noise level of HPD in pulse height is larger than that of B&L PMT and the threshold level of HPD is set higher than that of B&L PMT. There are flat regions between pedestal and 1p.e. or 1p.e. and 2p.e. peaks due to the contamination of photo-electron backscattering on the AD. Therefore, the backscattering signals which pulse height are lower than threshold level become undetectable and these reduce the trigger efficiency of HPD. It is necessary to reduce the noise of preamplifier in order to solve this problem.

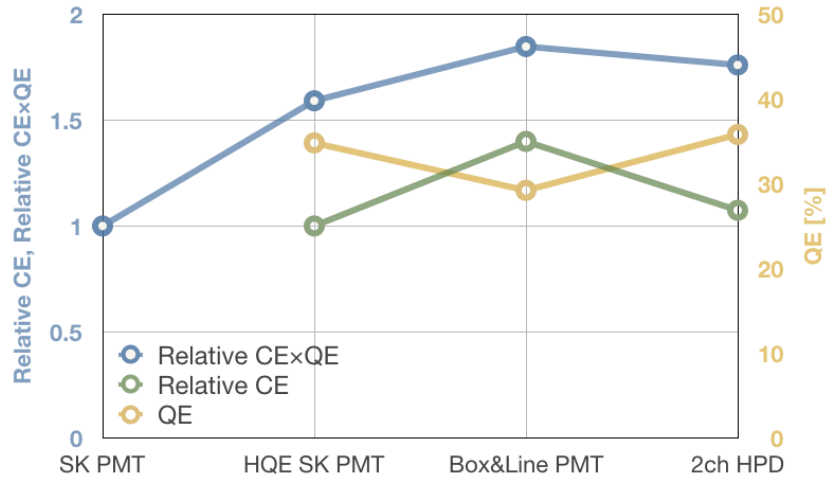


Figure 4.15: The measured relative total detection efficiency (= relative collection efficiency (CE)  $\times$  quantum efficiency (QE)), QE measured by Hamamatsu photonics and calculated relative CE.

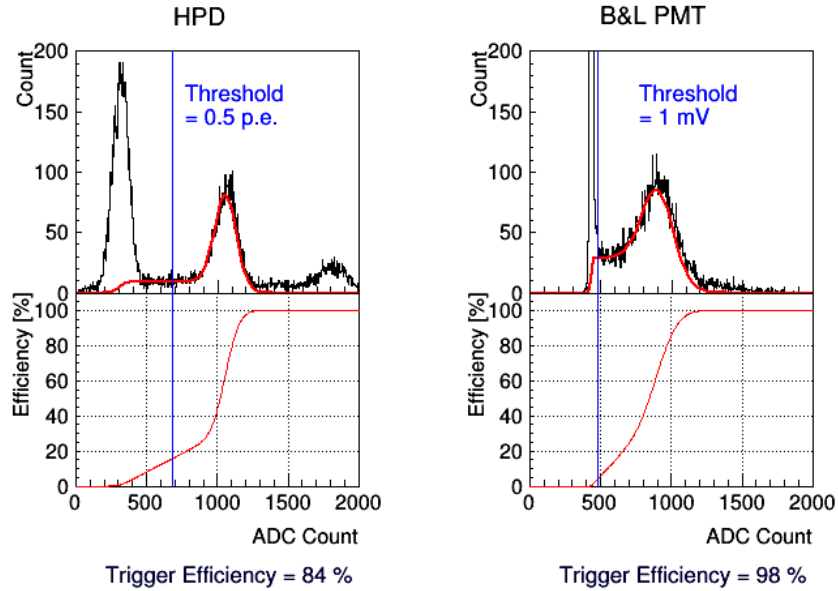


Figure 4.16: The charge distribution and trigger efficiency of an HPD and a B&L PMT.

## 4.8 Afterpulse

Afterpulse of a large aperture HPD or PMT occurs  $O(1)\sim O(10)$   $\mu s$  after the initial photoelectron signal and becomes the background especially for low rate event detection like Michel electron. The cause of afterpulse is positive ion generated by photo-electron and residual gases in glass. In HPD, There are no multiplied electrons between dynodes like PMTs, therefore it is considered that the possibility of generating positive ion becomes much lower and the afterpulse rate is less than that of PMTs.

We measured afterpulse rate by counting signals between  $-5$  to  $50$   $\mu s$  time windows by TDC. Fig. 4.17 shows the count rate normalized by the main pulse counts in each 500 ns window. The existence of negative rate point is due to subtraction of dark count rate. Table 4.4 shows the sum of the normalized count rate between  $0.5$  to  $50$   $\mu s$ . The afterpulse rate of HPD is the same level of SK PMT and less than that of B&L PMTs<sup>2</sup>.

<sup>2</sup>The data of B&L PMTs is measured at 2015. The recent developed B&L PMTs are more improved and have lower afterpulse rate.

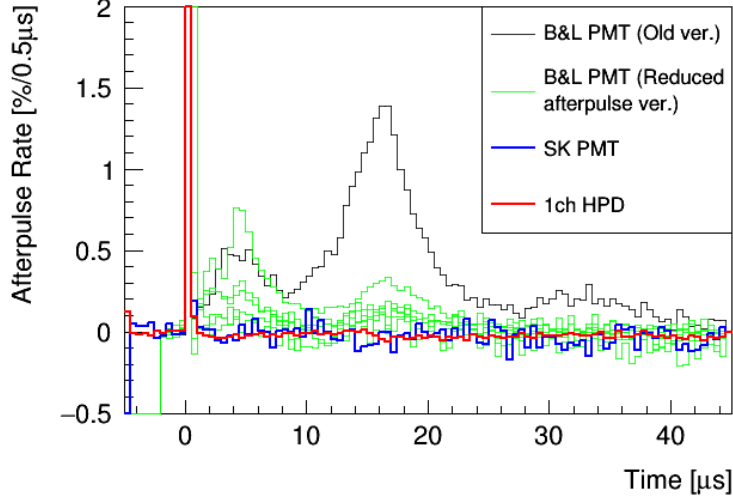


Figure 4.17: The afterpulse rate of each photodetector between  $-5$  to  $50 \mu\text{s}$  time windows from main pulse.

Table 4.4: The rate of afterpulse to mainpulse for each photodetector.

PD Type	Rate [%]
1ch HPD	$< 2.3$
SK PMT	$< 2.5$
B&L PMT (old ver.)	$\sim 30$
B&L PMT (reduced afterpulse ver.)	$1 \sim 13$

## 4.9 Rate tolerance

It is necessary for the photodetectors of HK to have sufficient high rate tolerance in order to detect the high rate event like a supernova explosion. If supernova explosion occurs at 10 kpc from the earth,  $O(100)$  kHz event rate in  $O(10)$  MeV energy is expected. This yield  $O(10^7)$  photons per second at the whole HK detector. Because the HK has forty thousand photodetectors per tank and mean number of detected photons per photodetectors is less than  $O(1)$  p.e. , it is considered that 1 MHz rate tolerance of photodetectors is sufficient for HK.

We measured the signal output stability of HPD by changing the frequency of input light pulse. As shown in Figure 4.18, the output is constant within 5% up to 1.2 MHz for 50 p.e. signal in charge. It is sufficient to detect the supernova burst events which is assumed in HK.

The cutoff frequency is limited by the pulse width of the preamplifier ( $\sim 100$

ns). In order to improve the rate tolerance of an HPD, it is necessary to make its fall time shorter and develop a quick response preamplifier. Below the cutoff frequency, the output of HPD slightly increases as the signal rate increases in both charge and pulse height. The reasons are considered as follows: First is the pile up due to the ringing of output pulse. It may cause the base line shift and we have to correct this effect. Second is the instability of the light source. In this measurement, we do not monitor the output of light source and there is a possibility to change the number of input photons. Third is the gain increase of the AD. It is planned to do more detail measurement.

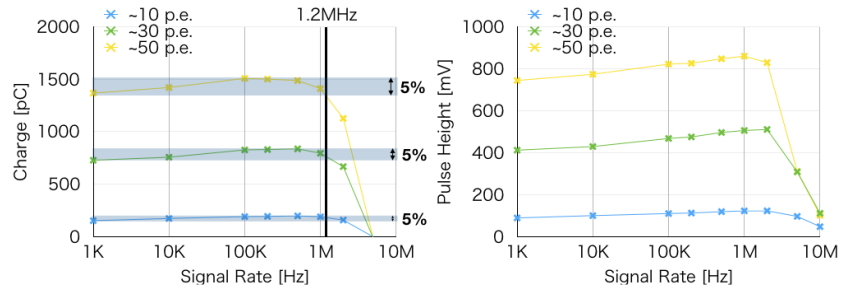


Figure 4.18: The output signal stability of HPD in charge and pulse height.

## 4.10 Viability test of an 50 cm HPD in water

Photodetectors for HK will be operated in water for 20 years. B&L PMTs and 20 cm HPDs are under the viability test [27] in EGADS (Evaluating Gadolinium's Action on Detector System), which is a 200-ton water tank in Kamioka mine as shown in Fig. 4.19 and 4.20. On the other hand, the long term performance stability of a 50 cm HPD has never been evaluated.

Because the basic performance of a prototype 50 cm HPD is confirmed, we move to the viability test in water as the next step. We make a waterproof 50 cm HPD in July 2016 and do the performance test in water as shown in Fig. 4.21. Fig. 4.22 shows 1 p.e. and multi p.e. signal of a waterproof 50 cm HPD. The noise level of a waterproof HPD is the same as a prototype 50 cm HPD and we can separate each photoelectron signal clearly (Fig. 4.23).

We conduct a continuous operation test in dark box filled with water for 20 days in the end of July and confirmed no trouble and stable operation. Fig. 4.24 shows the variation of dark rate and water temperature during continuous operation of a waterproof HPD. For the initial period of the operation, the dark rate changes because of the stabilization of the photodetector and the temperature change. After the temperature is stabilized, the HPD works stably. Fig. 4.25 shows the relationship of a temperature and a dark rate of a waterproof HPD. It was confirmed that the dark rate of an HPD at a water temperature ( $\sim 15^\circ\text{C}$ ) in HK becomes half of that at a normal temperature ( $\sim 25^\circ\text{C}$ ).

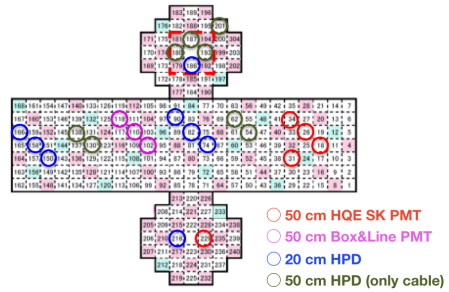
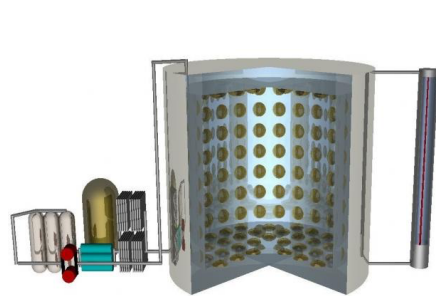


Figure 4.19: The schematic view of EGADS tank (a 200-ton water tank).

Figure 4.20: The extend elevation of EGADS tank. Green circles show the places planning to install 50 cm HPDs.



Figure 4.21: The waterproof HPDs and the picture of operation in water.

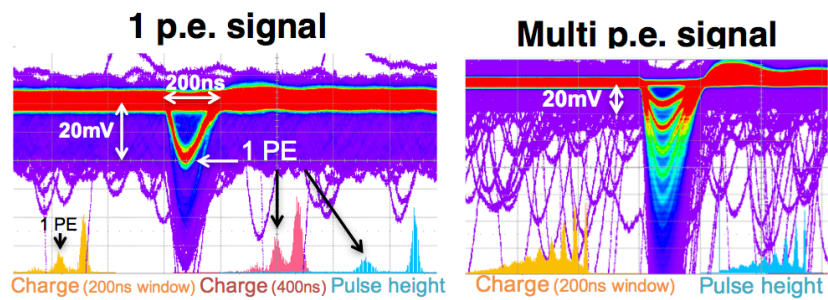


Figure 4.22: 1 p.e. and multi p.e. signal of a waterproof 50 cm HPD.

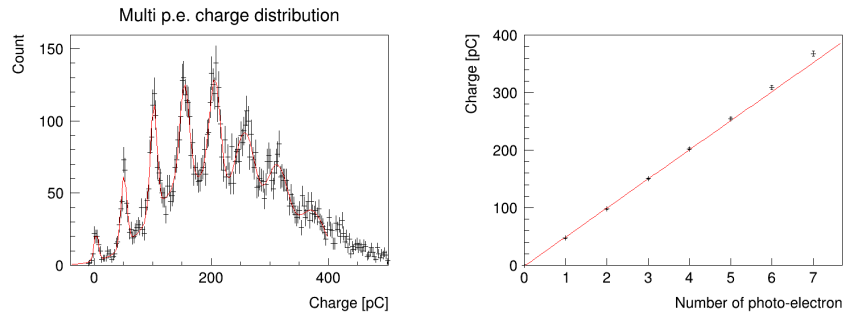


Figure 4.23: The multi p.e. charge distribution of a waterproof 50 cm HPD and charge of each number of photo-electron peaks.

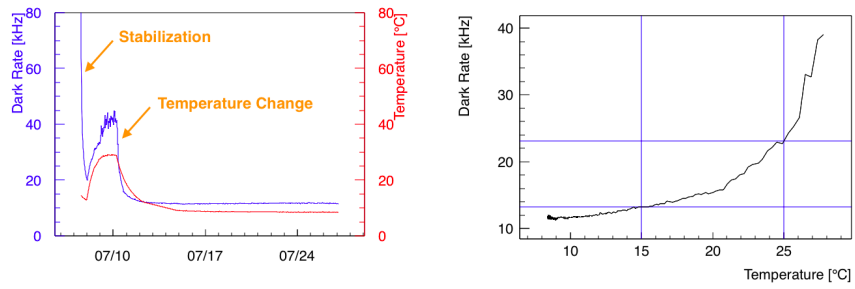


Figure 4.24: The variation of dark rate and temperature during continuous operation of a waterproof HPD. Figure 4.25: The relationship of a temperature and a dark rate of a waterproof HPD.

# Chapter 5

## Conclusion

### 5.1 Summary of performance evaluation

We have developed the prototype of the large aperture diameter HPD and confirmed its basic performance. The evaluated performance and comparison with other photodetectors are summarized in Table 5.1.

The charge resolution of an HPD is 17.7% which satisfy the requirement and timing resolution is 2.7 ns in TTS (FWHM) which reaches the required value. They are better than other candidate photodetectors. The dark rate of an HPD is  $\sim 10$  kHz at the room temperature. It is expected to reach the HK requirement ( $\sim 4$  kHz) at the water temperature supposed for HK operation. The afterpulse rate is less than 2.5% and it satisfy the requirement. It is better than that of B&L PMT and the same level as SK PMT. The single photon detection efficiency is measured relatively and confirmed that it is better than that of SK PMT and the same level as B&L PMT. It clears the requirement. An HPD has the rate tolerance up to 1.2 MHz. It is less than the required value, but the required value is conservative and 1 MHz rate tolerance is sufficient to detect any supernova burst events. In order to confirm the waterproof assembly of an 50 cm HPD for future long operation in water, we do the waterproof HPD test and it works stably for two weeks with applying high voltage.

Table 5.1: The summary of the evaluated performances of the 50 cm HPDs and comparison with SK PMT and B&L PMT.

	Required Value	SK PMT	B&L PMT	HPD
Rise Time [ns]	-	10.6	7.6	13.4
Fall Time [ns]	-	13.2	16.0	59.2
FWHM [ns]	-	18.8	12.2	41.3
Charge resolution [%]	~50	53	35	17.7
Timing resolution [ns]	~2.4	7.0	4.0	2.7 <sup>i</sup>
Dark rate [kHz]	~4	4 <sup>ii</sup>	8 <sup>iii</sup>	10 <sup>iv</sup>
Afterpulse [%]	< 15%	1 ~ 13	< 2.3	< 2.5
Detection efficiency (relative)	1	1	1.85	1.76
Rate tolerance [MHz]	10	-	87	1.2

## 5.2 Remaining issues

For the requirement mentioned Section 2, dynamic range, magnetic field tolerance, lifetime and pressure rating is not evaluated in this thesis. The output of the 50 cm HPD is linear up to 100 photoelectron signals. This output limit of an HPD comes from the operating voltage of the preamplifier. The dynamic range will be improved in a next version of the preamplifier. The magnetic field tolerance is evaluated by other measurement [28]. The lifetime will be evaluated in the future long term validity test in water. To test the pressure rating, we can use existing facilities which is used for the pressure rating test of B&L PMT and the procedure is established.

Additionally, to make an 50 cm HPD practical for use in a water Cherenkov detector, there are several remaining issues.

### Cathode transit time difference

The cathode transit time difference (CTTD) of 50 cm HPD is not uniform. There are about 2 ns fluctuations. To improve the CTTD of an HPD, it is necessary to redesign the shape of the glass bulb. Current shape of the 50 cm HPD is the same as that of 50 cm B&L PMT and it is not optimized for a 50 cm HPD. Because the structure of an HPD is simpler and the number of components is less than that of a PMT, the short bulb shape as shown in Fig. 5.1 is suitable for an HPD. By optimizing the shape of the glass bulb, we can improve not only CTTD but also collection efficiency and magnetic field tolerance.

<sup>i</sup>at the maximum AD bias voltage ( $\sim 570$  V).

<sup>ii</sup>at water temperature ( $\sim 16^\circ\text{C}$ ).

<sup>iii</sup>at water temperature ( $\sim 16^\circ\text{C}$ ).

<sup>iv</sup>at room temperature ( $\sim 25^\circ\text{C}$ ).

## Flasher

An HPD emits photons and becomes a flasher. A flasher becomes background in a water Cherenkov detector and has a bad influence on other photodetectors. The mechanism of HPD flasher is considered such that electrons are emitted from the aluminum vapor-deposited on an end surface, creeping the surface of the bulb, shot to the stem of the bulb to generate photons. To solve this problem, it is proposed that chromium is vapor deposited on an end surface and suppress the electron emission.

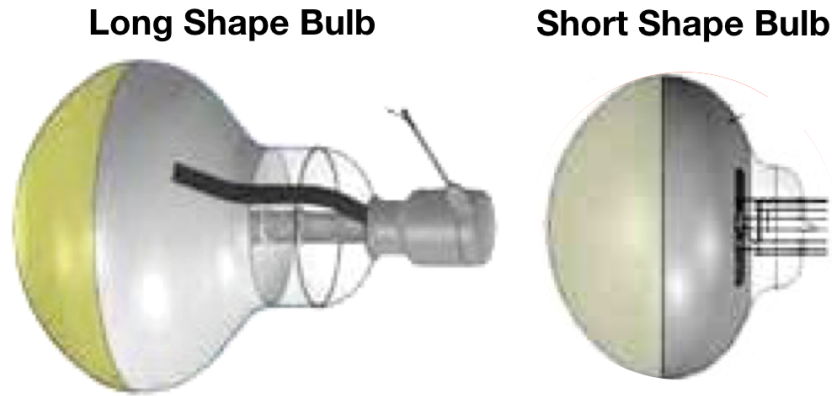


Figure 5.1: The shape of the glass bulb.

## 5.3 Future prospect

An HPD can satisfy the basic requirement for HK except for dynamic range. It is improved for the next version of the preamplifier. Additionally, there are room to improve other performances of the preamplifier. By tuning parameters and reducing the noise of preamplifier signal output, the timing resolution can be improved and the lower threshold level can be set which result in increasing the single photon collection efficiency. It enhances the sensitivity of short time or low energy physics events like the  $p \rightarrow \bar{\nu} K^+$  mode because the lifetime of the kaon is  $\sim 12$  ns and the energy of the nuclear de-excitation  $\gamma$  ray is  $\sim 6.3$  MeV. By making the fall time of the signal waveform shorter, the rate tolerance will be improved. It makes possible to observe the supernova explosion near the earth and study the mechanism more precisely.

It is necessary to study which configuration is most suitable for HPD to use in HK. 1ch HPD and single channel read-out is assumed to have higher collection efficiency because of no insensible field on the AD due to no segment meshes and lower amount of DAQ data than multi-channel HPD. On the other hand, the multi-channel HPD, especially for 5ch HPD, and each channel read-out is assumed to have the position sensitivity on the photocathode because the incident photon which hit the center (surrounding) of the photocathode is likely

to be collected to the center (surrounding) of the AD. By using this information, it is considered that we can study the event near the tank wall more precisely and expand the fiducial volume of HK. These studies are ongoing[28] and will be continue.

The most influential factor to make a 50 cm HPD practicable is to eliminate flasher. Therefor, we plan to perform R&D for suppressing flasher and this will be finished in one year. After the elimination of flasher, we will do the validity test for a long term in water to ensure that an HPD is suitable to be used in a water Cherenkov detector.

# Acknowledgements

I would like to express the deepest appreciation to Prof. Masashi Yokoyama for giving an opportunity to research in high energy physics and his support in my studies.

I owe a very important debt to Dr. Yasuhiro Nishimura for teaching how to operate HPD and take data, Dr. Akimichi Taketa for teaching how to design and fabricate the preamplifier of HPD.

Special thanks to the members of Hamamatsu Photonics K.K., Dr. Yoshihiko Kawai, Takayuki Ohmura and Masatoshi Suzuki, especially for the development of HPD.

I am deeply grateful to the staff of Kamioka, Prof. Masato Shiozawa, Prof. Yoshinari Hayato, Dr. Hidekazu Tanaka, Dr. Shoei Nakayama, Dr. Takatomi Yano for the help of the research in Kamioka and supervision.

Many thanks to the student at Kamioka, Seiko Hirota, Yuji Okajima, Daisuke Fukuda, Miao Jiang, Ryosuke Akutsu, Fumimasa Muto, Yutaro Sonoda for the enjoyable life in Kamioka. Without their help, I could not perform my research in Kamioka.

I would like to thank the members in Aihara-Yokoyama laboratory, Prof. Hiroaki Aihara, Dr. Yoshiyuki Onuki, Nobuhiro Shimizu, Yusuke Suda, Taichiro Koga, Junya Sasaki, Yifan Jin, Fuminao Hosomi, Hiroko Niikura, Naruhiro Chikuma, Alejandro Mora Grimaldo Johnny, Wan Kun, Tatsuki Ose, Riku Tamura for my fruitful life in Hongo. I also would like to thank Kuniko Kono who supports our laboratory for her fantastic assist.

Finally, I would like to express my gratitude to my parents for continuously supporting and encouraging me.

## Appendix A

# Long term measurement of dark rate of Hyper-K photodetectors

As a candidate of photodetector for Hyper-K, the B&L PMT is well established and satisfies the performance requirements except for the dark rate. The dark rate of photodetectors is one of the most important factor to determine the whole HK detector performance, especially for the newly developed reconstruction algorithm like neutron tagging [29].

The dark rate of a PMT depends on the applied high voltage, the trigger threshold level, the temperature and the period kept in a dark environment. In order to study whether the dark rate of B&L PMT decreases after a long operation in a dark room and the effects of threshold and temperature, we have performed a long-term measurement of PMTs at an underground room in ICRR, Kashiwa, from the end of 2015.

### A.1 Setup

Fig. A.1 and A.2 show the setup in the dark room. The photodetectors are stored in a cardboard case and located in a shelf. A light source is installed in front of each photodetector and we can measure the dark rate and charge simultaneously. The temperature can be controlled by the air-conditioning system of the dark room.

Table A.1 shows the summary of photodetectors used in this long measurement. The measurement can be divided into two terms by installed photodetectors. First term is from October 2015. We use two SK PMTs and two B&L PMTs. Second term is from August 2016. We installed additional five newly developed B&L PMTs.

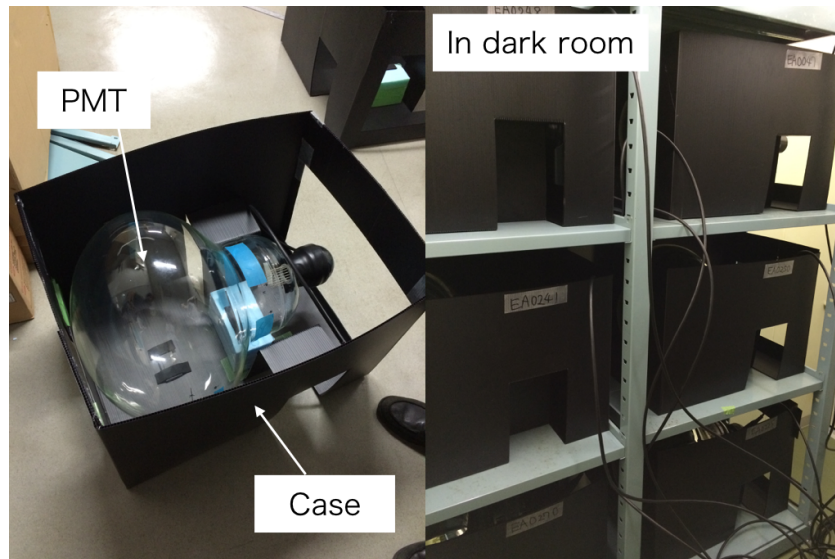


Figure A.1: Image of setup in dark room.

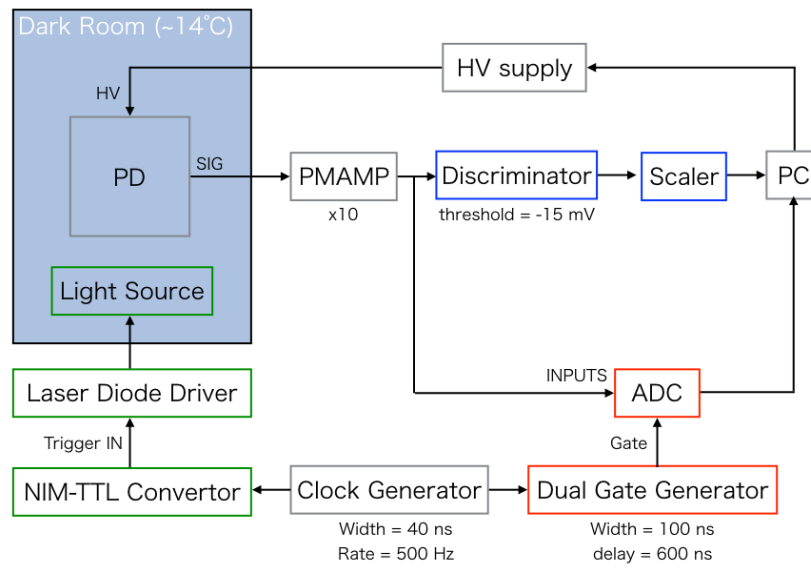


Figure A.2: The setup of DAQ system for long measurement.

## A.2 Result from October 2015 to September 2016

Fig. A.3 shows the time variation of gain and dark rate of photodetectors from October 2015 to September 2016. The discontinuity around May 2016 is due to the change of applied high voltages to match the gain of photodetectors to the criterion used in SK (1 p.e.  $\sim 2.2$  pC, gain  $\sim 1.4 \times 10^7$ ). After changing the HV, the gain and dark rate of photodetectors are stabilized.

In table A.1, the averaged dark rate is summarized. After about half a year operation in a dark room with applying high voltage, the dark rate of SK PMTs (CD9092 and AB7836) become around 5 kHz, which are the same level of PMTs in SK, while that of B&L PMTs (EA0047 and ZB8208) is more than 10 kHz and does not satisfy the requirements of HK.

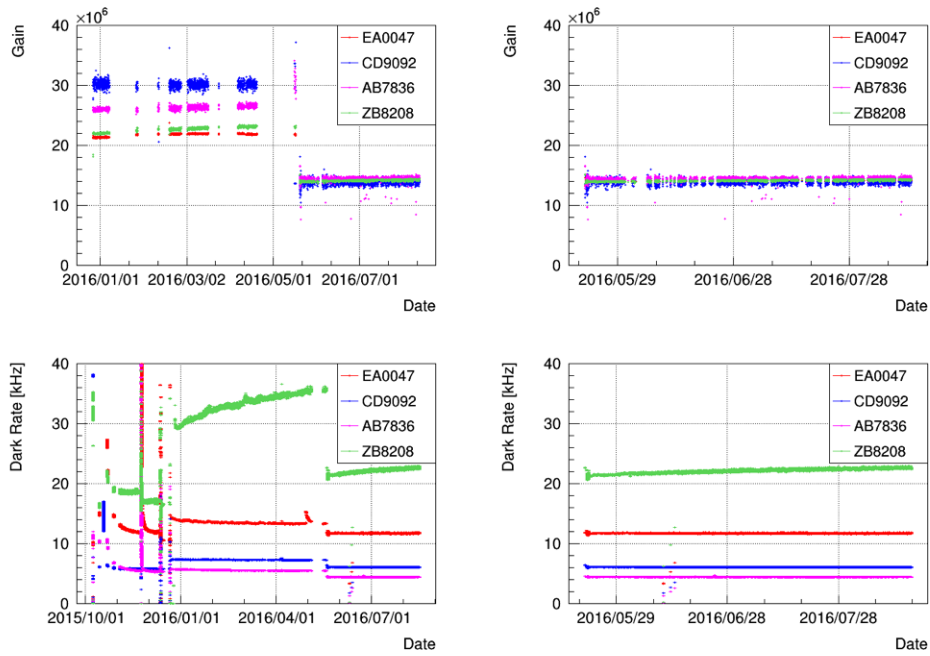


Figure A.3: The time variation of gain (upper) and dark rate (lower). The left column shows the whole history of gain and dark rate and the right column shows the history after May 2016.

### A.3 Result from August 2016 to November 2016

Fig. A.4 shows the variation of the dark rate after installing additional five B&L PMTs. Until the end of August 2016, the dark rates had been changing due to stabilization. The variation at the beginning of September is caused by the change of the temperature in the dark room. After September 8, the dark rates stabilized. The averaged dark rate of newly installed PMTs is 7.6 kHz and improved compared with old versions, but does not reach the HK requirement ( $\sim 4$  kHz).

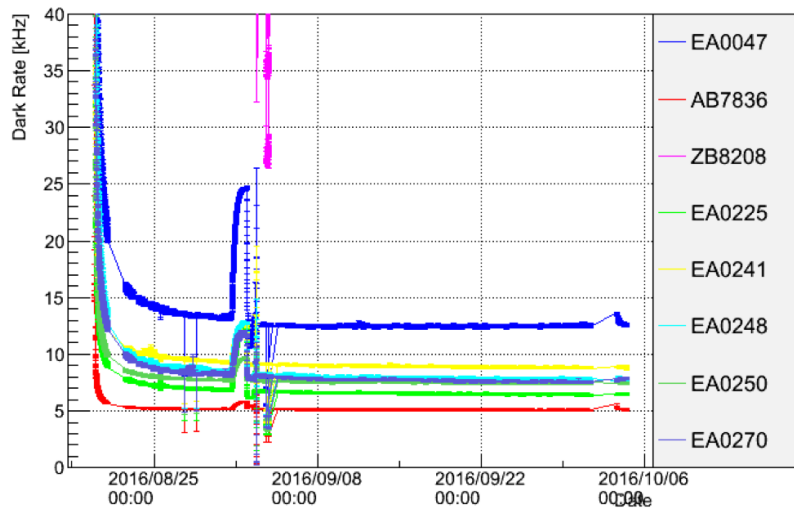


Figure A.4: The time variation of the dark rate after installing newly developed B&L PMTs

Table A.1: Summary of the type of measured photodetectors and averaged dark rate after stabilization. WPASSY is short for waterproof assembly.

Serial No.	Type	Installed time	Averaged dark rate [kHz]
AB7836	SK PMT	October 2015	4.4
CD9092	"	"	6.1
ZB8208	B&L PMT	"	21.7
EA0047	"	"	11.7
EA0225	B&LPMT WPASSY	August 2016	6.5
EA0241	"	"	8.8
EA0248	"	"	7.8
EA0250	"	"	7.4
EA0270	"	"	7.6

We measure the temperature dependence of dark rate using the temperature changing period. The results are shown in Fig. A.5. We also measure the high voltage and trigger threshold level dependence of the dark rate as shown in Fig. A.6. By cooling a PMT, the dark rate of a PMT decreases in accordance with Richardson’s law for thermionic emission

$$r_R(T) = AT^2 \exp\left(-\frac{W}{kT}\right) \quad (\text{A.1})$$

while when the temperature goes below zero degree celsius, non-thermal effects becomes non-negligible and the dark rate follows

$$r_{nt}(T) = GA_c \exp\left(-\frac{T}{T_r}\right) \quad (\text{A.2})$$

where A is a normalization factor, W is work function [eV], k is the Boltzmann constant ( $= 8.617$  [eV/K]), G is an empirical constant ( $= 5 \pm 1$  [kHz/cm<sup>2</sup>]), A<sub>c</sub> is the cathode area [cm<sup>2</sup>] and T<sub>r</sub> is the adjusted slope of the data ( $= 100$  [K]) [30].

To reduce the dark rate by half, we are improving B&L PMTs with Hamamatsu Photonics. The dark rate is evaluated roughly in Hamamatsu for a few weeks and precisely in Kashiwa for the period of monthly basis. The environment of these two measurement is different. Therefore, we are planning to fill the gap by using the data of dark rate dependence on the temperature, high voltage and threshold level.

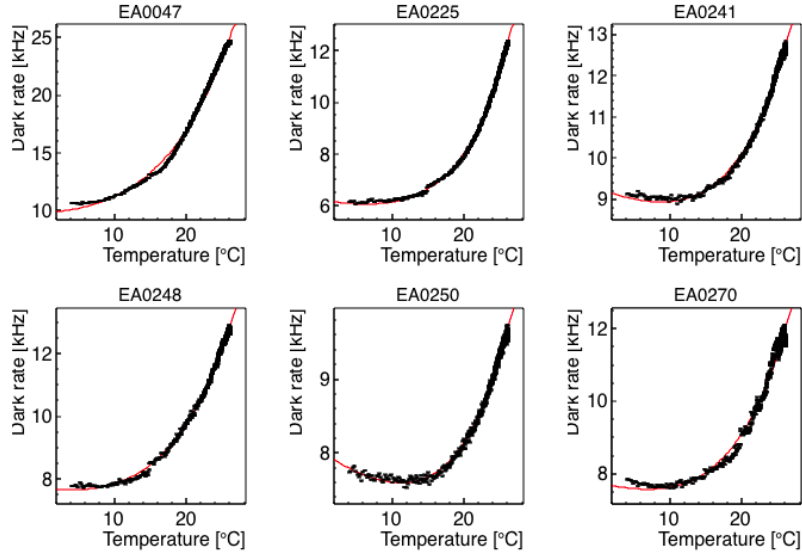


Figure A.5: The temperature dependency of PMT dark rate.

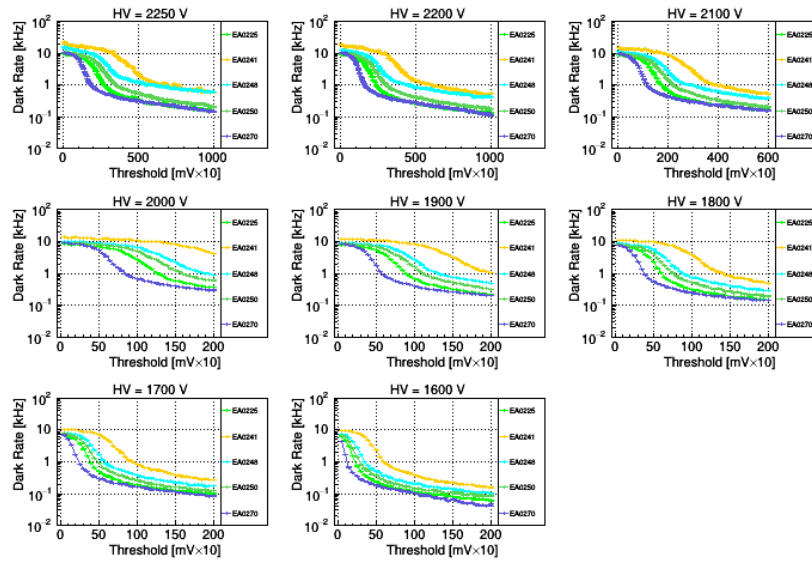


Figure A.6: The high voltage and trigger threshold level dependency of the dark rate.

# Bibliography

- [1] Ziro Maki, Masami Nakagawa, and Shoichi Sakata. [Remarks on the Unified Model of Elementary Particles](#). *Progress of Theoretical Physics*, 28(5):870–880, 1962.
- [2] K. Abe et al. [Solar neutrino measurements in Super-Kamiokande-IV](#). *Phys. Rev. D*, 94:052010, Sep 2016.
- [3] S. Abe et al. [Precision Measurement of Neutrino Oscillation Parameters with KamLAND](#). *Phys. Rev. Lett.*, 100:221803, Jun 2008.
- [4] A. Gando et al. [Reactor on-off antineutrino measurement with KamLAND](#). *Phys. Rev. D*, 88:033001, Aug 2013.
- [5] Y. Ashie et al. [Measurement of atmospheric neutrino oscillation parameters by Super-Kamiokande I](#). *Phys. Rev. D*, 71:112005, Jun 2005.
- [6] M. G. Aartsen et al. [Determining neutrino oscillation parameters from atmospheric muon neutrino disappearance with three years of IceCube DeepCore data](#). *Phys. Rev. D*, 91:072004, Apr 2015.
- [7] K. Abe et al. [Measurements of neutrino oscillation in appearance and disappearance channels by the T2K experiment with  \$6.6 \times 10^{20}\$  protons on target](#). *Phys. Rev. D*, 91:072010, Apr 2015.
- [8] P. Adamson et al. [Measurement of Neutrino and Antineutrino Oscillations Using Beam and Atmospheric Data in MINOS](#). *Phys. Rev. Lett.*, 110:251801, Jun 2013.
- [9] P. Adamson et al. [First measurement of muon-neutrino disappearance in NOvA](#). *Phys. Rev. D*, 93:051104, Mar 2016.
- [10] F. P. An et al. [Spectral Measurement of Electron Antineutrino Oscillation Amplitude and Frequency at Daya Bay](#). *Phys. Rev. Lett.*, 112:061801, Feb 2014.
- [11] K. Abe et al. [Evidence of electron neutrino appearance in a muon neutrino beam](#). *Phys. Rev. D*, 88:032002, Aug 2013.

- [12] S. P. Mikheyev and A. Yu. Smirnov. Resonance enhancement of oscillations in matter and solar neutrino spectroscopy. *Soviet Journal of Nuclear Physics.*, 42:913917, 1985.
- [13] L. Wolfenstein. [Neutrino oscillations in matter](#). *Phys. Rev. D*, 17:2369–2374, May 1978.
- [14] A. D. Sakharov. [Violation of CP invariance, C asymmetry, and baryon asymmetry of the universe](#). *Soviet Physics Uspekhi*, 34:392, 1991.
- [15] J. H. Christenson, J. W. Cronin, V. L. Fitch, and R. Turlay. [Evidence for the  \$2\pi\$  decay of the  \$k\_2^0\$  meson](#). *Phys. Rev. Lett.*, 13:138–140, Jul 1964.
- [16] A. J. Bevan et al. The Physics of the B Factories. *arXiv:1406.6311*.
- [17] M. Miura. [Search for Proton Decay via  \$p \rightarrow e^+\pi^0\$  and  \$p \rightarrow \mu^+\pi^0\$  in 0.31 megaton-years exposure of the Super-Kamiokande Water Cherenkov Detector](#). 2016.
- [18] K. et al. Abe. [Search for proton decay via  \$p \rightarrow \nu K^+\$  using 260 kiloton-year data of Super-Kamiokande](#). *Phys. Rev. D*, 90:072005, Oct 2014.
- [19] K. Abe et al. [Letter of Intent: The Hyper-Kamiokande Experiment — Detector Design and Physics Potential](#) —. 2011.
- [20] Y. Suda et al. [Performance evaluation of the large-aperture Hybrid Photo-Detector](#). 2014.
- [21] S. Hirota et al. [New large aperture, hybrid photo-detector and photo multiplier tube for a gigantic water Cherenkov ring imaging detector](#). 2014.
- [22] M. Jiang et al. [The development and performance evaluation of a hybrid photo-detector for Hyper-Kamiokande](#). 2015.
- [23] E. Gatti, P.F. Manfredi, and D. Marioli. [Limitations in transformer coupling between radiation detector and head amplifier](#). *Nuclear Instruments and Methods in Physics Research*, 193(3):539 – 547, 1982.
- [24] Miao Jiang. Research and Development of Large-Aperture Hybrid Photo-Detector for Hyper-Kamiokande. Master’s thesis, Kyoto University, 2015.
- [25] Y. Okajima et al. [Detailed performance evaluation of a new 20-inch photomultiplier tube with a Box and Line dynode](#). 2015.
- [26] Hirokazu Ikeda, Masaki Mori, Tohru Tanimori, Ken ichi Kihara, Yoichiro Suzuki, and Yasuhiko Haren. [Front-end hybrid circuit for super-KAMIOKANDE](#). *Nuclear Instruments and Methods in Physics Research Section A: Accelerators, Spectrometers, Detectors and Associated Equipment*, 320(1):310 – 316, 1992.

- [27] S. Hirota et al. [New large aperture, hybrid photo-detector and photo multiplier tube for a gigantic water Cherenkov ring imaging detector](#). *Nuclear Instruments and Methods in Physics Research Section A: Accelerators, Spectrometers, Detectors and Associated Equipment*, 766:152 – 155, 2014. {RICH2013} Proceedings of the Eighth International Workshop on Ring Imaging Cherenkov Detectors Shonan, Kanagawa, Japan, December 2-6, 2013.
- [28] Fumimasa Muto. [ハイパーカミオカンデ実験のための新型光検出器の性能評価](#). Master's thesis, Nagoya University, 2017.
- [29] H. Watanabe et al. [First study of neutron tagging with a water Cherenkov detector](#). *Astroparticle Physics*, 31(4):320 – 328, 2009.
- [30] H. O. Meyer. [Dark Rate of a Photomultiplier at Cryogenic Temperatures](#). 2008.